catalysts

MDPI

Review

Engineered 2D Metal Oxides for Photocatalysis as Environmental Remediation: A Theoretical Perspective

Ali Raza [1,†], Yifei Zhang [2,†], Antonio Cassinese [1,*] and Gao Li [3,*]

[1] Department of Physics, University of Naples "Federico II", Piazzale Tecchio, 80, 80125 Naples, Italy
[2] Institute of Catalysis for Energy and Environment, College of Chemistry and Chemical Engineering, Shenyang Normal University, Shenyang 110034, China
[3] State Key Laboratory of Catalysis, Dalian Institute of Chemical Physics, Chinese Academy of Sciences, Dalian 116023, China
* Correspondence: antonio.cassinese@unina.it (A.C.); gaoli@dicp.ac.cn (G.L.)
† These authors contributed equally to this work.

Abstract: Modern-day society requires advanced technologies based on renewable and sustainable energy resources to meet environmental remediation challenges. Solar-inspired photocatalytic applications such as water splitting, hydrogen evolution reaction (HER), and carbon dioxide reduction reaction (CO_2RR) are unique solutions based on green and efficient technologies. Considering the special electronic features and larger surface area, two-dimensional (2D) materials, especially metal oxides (MOs), have been broadly explored for the abovementioned applications in the past few years. However, their photocatalytic potential has not been optimized yet to the level required for practical and commercial applications. Among many strategies available, defect engineering, including cation and anion vacancy creations, can potentially boost the photocatalytic performance of 2D MOs. This mini-review covers recent advancements in 2D engineered materials for various photocatalysis applications such as H_2O_2 oxidation, HER, and CO_2RR for environmental remediation from theoretical perspectives. By thoroughly addressing the fundamental aspects, recent developments, and associated challenges—the author's recommendations in compliance with future challenges and prospects will pave the way for readers.

Keywords: 2D metal oxides; environmental remediation; defect engineering; water oxidation; H_2 evolution; CO_2 reduction

check for updates

Citation: Raza, A.; Zhang, Y.; Cassinese, A.; Li, G. Engineered 2D Metal Oxides for Photocatalysis as Environmental Remediation: A Theoretical Perspective. *Catalysts* **2022**, *12*, 1613. https://doi.org/10.3390/catal12121613

Academic Editor: Hamidreza Arandiyan

Received: 2 October 2022
Accepted: 2 December 2022
Published: 8 December 2022

1. Introduction

Numerous MOs have large bandgap energies, which provide attractive energy levels for redox reactions but frequently suffer from poor electron conductivity, reducing photocatalytic frequencies. Given the difficulty of accelerating the transfer of photogenerated electrons in pure MOs, reducing the migration direction will be a more efficient way to boost photocatalysis. Therefore, we can shrink the third dimension while extending the scale of the remaining two dimensions, resulting in a thin assembly with a large surface fraction. This 2D structure minimizes the distance between bulk and surface-active sites for electron migration and maintains a high specific surface area. Certainly, fabricating MOs based on 2D materials is a cost-effective method for optimizing surface area and charge transfer, thus achieving a proficient photocatalytic efficiency [1]. Because most MOs lack layered architectures, only a few 2D MOs were first recognized for photocatalysis. However, with the development of new synthetic approaches and procedures, 2D nanostructures, such as TiO_2, Fe_2O_3, Cu_2O, ZnO, WO_3, SnO, In_2O_3, CeO_2, and HNb_3O_8, were developed and applied to photocatalysis [2,3]. Because of their non-layered structures, several 2D MOs are challenging to shape using the straightforward ultrasonic exfoliation technique. As a result, several other techniques were used to control the shape of such materials. For instance, a lamellar organic/inorganic hybrid approach has been suggested to fabricate

ultrathin TiO_2 nanostructures [2]. The solvothermal method was used to produce lamellar TiO_2 octylamine hybrid precursors using Ti isopropoxide (Ti source), octylamine (capping reagent), and 2-phenyl ethanol (solvent) (Figure 1a–c) [1,4]. The powder obtained from the ultrasound-based exfoliation was washed to remove octylamine and obtain smooth, ultrathin (~98 nm) TiO_2 nanostructures.

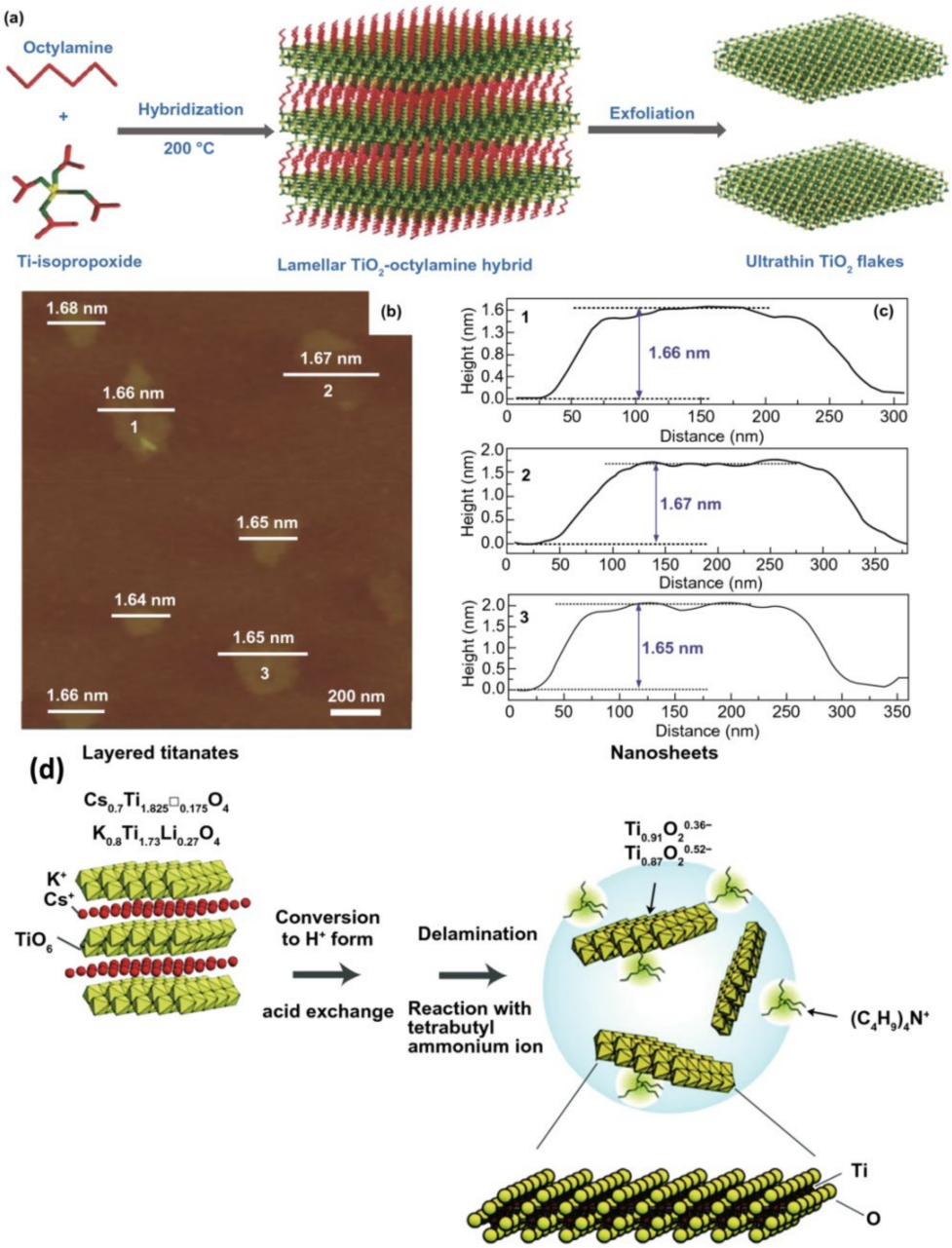

Figure 1. Flakes of ultrathin TiO_2: (**a**) Synthesis scheme, adapted from [2] Copyright 2016 Elsevier B.V.; (**b**) AFM image; (**c**) AFM images of height profiles in (**b**), adapted from [1] Copyright 2018, John Wiley & Sons; (**d**) exfoliation of titanate crystals of the lepidocrocite type into TiO_2 nanostructures is depicted schematically, adapted from [5] Copyright 2016, The Royal Society of Chemistry.

Additionally, $Bi_2W_2O_9$ was exfoliated to achieve single-crystalline nanostructures. Due to the layered composition of $Bi_2W_2O_9$ ($[Bi_2O_2]^{2+}$ and $[W_2O_7]^{2-}$ layers), layers of WO_3 were obtained by carefully etching the $[Bi_2O_2]^{2+}$ layers with acids and stabilizing the layers of WO_3 with a surfactant (tetrabutylammonium hydroxide). These exfoliated WO_3 nanostructures had a higher bandgap than bulk WO_3, which was attributed to the quantum

confinement effect. Besides an exfoliation process, wet chemical techniques were used to prepare MOs nanostructures directly. Several ultrathin MOs have been developed using a self-assembly technique involving ethylene glycol (co-surfactant) and polyethylene oxide–polypropylene oxide–polyethylene oxide [1]. These MOs include TiO_2, Fe_3O_4, Co_3O_4, ZnO, MnO_2, and WO_3. Furthermore, perovskite oxides have recently experienced a renaissance because of their improved efficiency in photocatalysis and solar cell applications. In order to produce their layered perovskite nanosheets, numerous stratiform perovskites can be easily exfoliated [1].

Various MOs, such as SnO_2, WO_3, TiO_2, Fe_2O_3, and ZnO, have been broadly examined as photocatalysts over the last four decades [6,7]. TiO_2 was the most studied because of its high stability, adequate electronic structure, biocompatibility, and superior light absorption properties. The 2D nanostructures of TiO_2 obtained by exfoliating layered titanate have attracted interest for their potential use as photocatalysts [8]. These nanostructures exhibit semiconducting properties such as their bulk counterparts and contain anatase and rutile phases but with somewhat higher bandgap due to confinement effects. $Ti_{0.91}O_{20.36}$ nanostructures, for example, demonstrated an energy gap value of 3.8 eV, which was greater when compared to anatase titania (3.2 eV) [9]. The top-down multistep process was well known for the exfoliation and intercalation of layered MOs to form their bulk counterparts [10]. For instance, layered titanates were initially developed in the case of TiO_2 nanostructures through a traditional solid-state reaction between an alkali metal carbonate solution and TiO_2 at high temperatures (Figure 1d). Numerous layered MOs, including titanoniobate (Ti_5NbO_{14}, Ti_2NbO_7, and $TiNbO_5$), perovskite oxides ($KLnNb_2O_7$ and $RbLnTa_2O_7$), $HCa_{2-x}Sr_xNb_3$, HNb_3O_8, and WO_3 were fabricated via similar solid-state reactions and wet-chemical exfoliation approaches [11–13]. Zhou et al. recently developed freestanding, single-layer Bi_2WO_6 nanostructures from cetyltrimethylammonium bromide using a wet chemical method. Several active sites were generated on the surface of the single-layer nanostructures since Bi atoms were not saturated on the single layer, which directly produced holes upon light irradiation. Quick exciton separation at a highly photoactive surface revealed that single layer Bi_2WO_6 has outstanding photocatalytic efficiency for photo degradation of Rhodamine B [14]. Titanoniobate nanostructures have shown improved photocatalytic efficiency in eliminating organic pollutants [15]. By using a simple wet chemical technique, Tae et al. recently investigated the development of multiple titanate nanostructures with diamond-like shapes with a typical lateral size of 30 nm [16]. The current review is arranged as follows; firstly, the defect engineering tools, such as anion and cation vacancy creations, are thoroughly discussed. Moreover, third section deals with emerging environmental remedies such as water splitting, HER, and CO_2 reduction via theoretical aspect. The last section gives brief summary with challenges and future recommendations.

Superiority of 2D Materials as Photocatalysts

Ultrathin 2D materials with single or few atom thicknesses (>5 nm) have a high surface atom ratio, large surface area, and intrinsic quantum confined electrons that exhibit extraordinary optical, mechanical, and electronic properties and have great potential for the research of transistors, catalysis, optoelectronic, conversion, and the energy storage devices [17–22]. These materials present unique physiochemical behavior such as electronic anisotropy, high surface activity, planar conductivity, and tunable energy structure [23]. With the decrease in thickness of bulk substances to the atomic level, atomic structures will go through the apparent distinctions, including length and angle of bonds, coordination number, formation of surface defects, and disordering of surface atoms. As a result, ultrathin 2D materials exhibit not only bulk properties but also new features. Semiconductor photocatalytic materials have gained interest as they give promising solutions for environmental pollution and energy storage [24–29]. These materials split the water into hydrogen and oxygen, eliminating pollutants and reduction in CO_2 by solar light as an external driving force [30–35]. Light absorption, migration, separation of charges, and surface redox

reactions are significant steps for photocatalysis. Upon exposure to irradiation, the photocatalysts absorb the light and produce electron–hole pairs in the conduction and valance band (CB and VB), respectively. These photogenerated electron–hole pairs diffuse to the surface of the material and then migrate to the active sites before the surface reactions. The recombination of charges happens; texture, crystal structure, particle size, and crystallinity affect the separation efficiency. In the end, target molecules adsorb on the material's surface and undergo charge injection and desorption to make ultimate products [36–40]. Currently, many semiconductors exist for photocatalysis with tunable electronic and crystal structures. Although remarkable achievements are made to optimize the photocatalysis process, many photocatalysts show relatively low photocatalytic performance, which depends on the rational design of such materials. Ultrathin materials have awakened a new aspect of this field because of the appropriate band structure. Ultrathin 2D configuration can harvest more ultraviolet-visible radiations and have a large specific surface area. However, the absorption of photons is very limited in bulk materials due to the reflection and transmission of grain boundaries [1,19,41–43]. Additionally, as atomic thickness decreases the migration distance, charge carriers quickly move to the surface area in 2D materials. It reduces the recombination possibility and enhances photocatalysis. Lastly, unique 2D structures with a high surface-atom ratio render many active sites for accelerating the reaction processes. Moreover, atomic escape energies become relatively small due to the decrease in thickness. Surface defects play a role in the target molecule adsorption, building strong interplay, super activation process, and charge transfer. These features help photocatalysts display various features and numbers of scientific reports in this regard [44–46]. It is urgent and desirable to present an inclusive review on this field to encourage further developments in this niche.

2. Defect Engineering

2.1. Anion Vacancies

The physiochemical properties and electronic structure of 2D materials are successfully modified using atomically thick oxygen vacancies (Vos), impacting catalytic efficiency [47]. The Vos are among the defects in transition-MOs that have received the most attention due to their low formation energy [48]. In addition to changing the electronic structure and carrier concentration, engineered V_O result supports the activation of molecules such as CO_2, N_2, and O_2 and improves photocatalytic efficiency. By using electrons transferred from the excited BiOBr of the N_2 molecule over the contact, the N_2 molecule could be successfully reduced to NH_3. In the assembly of BiOBr, a cluster of electrons for back transfer has been found by Zhang et al. These clustered electrons can modify the adsorbed N_2 molecule and produce N-atoms stretching (1.078 to 1.133 Å) for free molecular nitrogen [49].

Further, the introduction of V_O in the assembly of ZnAl-LDH (layered double hydroxides) promotes CO_2 activation, such as N_2 activation [50]. The formation of varied unsaturated coordinate Zn ions close to the V_Os caused an increase in the density of V_O, to be seen as the thickness of obtained product ranges from 210 to 2.7 nm, gradually decreasing. The production of surface defects (V_O and Ti^{3+}) in TiO_2 nanosheets was offered by Kong et al. via plasma engraving technique [51].

The electrical structure of the 2D TiO_2 nanosheets undergoes considerable variation due to the produced defects, with the bandgap energy reduced from 3.12 to 2.88 eV with CB and VB edge upshifting to create a defective site in the forbidden bandgap. Compared to pure TiO_2, the H_2 production activity increased drastically due to the creation of this defective state. The V_O in WO_3 atomic layers stimulates the formation of intermediate bands in the bandgap and the adsorption and activation of CO_2 into radical COOH• species [52]. More CO and O_2 are produced in the infrared range due to the crucial role played by V_O in WO_3 layers. Lei et al. accomplished the regulated synthesis of V_O-rich and V_O-deficient In_2O_3 nanostructures via quickly heating $In(OH)_3$ nanostructures in an oxygen-rich atmosphere [53]. The atomic force microscopy (AFM) image in Figure 2 showed that the In_2O_3 nanostructures thickness was about 0.9 nm, demonstrating the controlled atomic

thickness of In_2O_3. Electron spin resonance (ESR) and X-ray photoelectron spectroscopy (XPS) spectra showed evidence of V_O. The production of ultrathin V_O-enriched In_2O_3 nanostructures with a peak maxima area was indicated by the 531.4 eV peaks, which also showed that more V_O-rich nanostructures were generated than V_O-poor ones or their equivalent bulk counterparts.

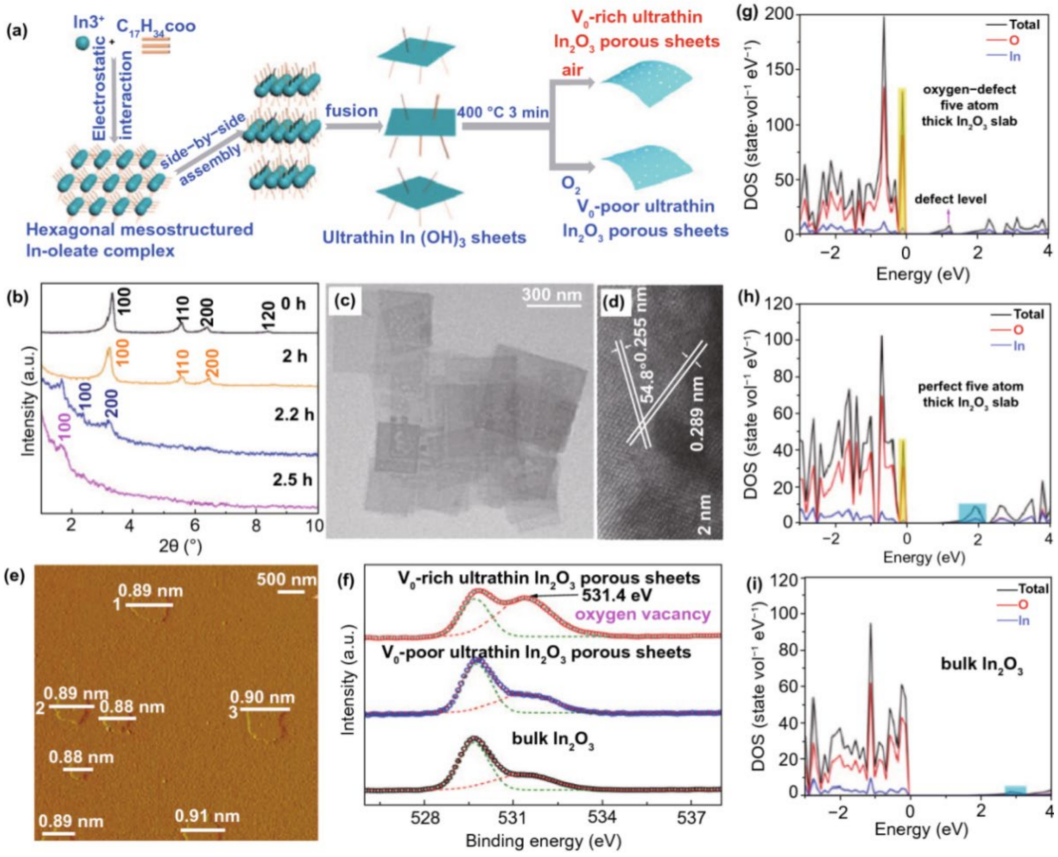

Figure 2. (**a**) Atomically thin In_2O_3 porous nanostructures with mixed V_O concentrations under specific conditions; (**b**) display of time-dependent small-angle X-ray diffraction patterns for an as-prepared precursor; (**c**–**f**) characterization of V_O-rich atomically thin, porous In_2O_3 nanostructures generated by air-based, rapid thermal heating of $In(OH)_3$ nanostructures; (**c**,**d**) demonstration of TEM/HR-TEM Photograph; (**e**) visualization of AFM investigation; (**f**) O 1s XPS spectra; (**g**) electron spins resonance spectrum; (**h**) simulated density of state (DOS) of an In_2O_3 slab with an O defect which is five atoms thick; (**i**) perfect In_2O_3 slab with a five-atom thickness. Adapted from [53] Copyright 2014, American Chemical Society.

Furthermore, higher V_O signals were seen in ESR at g = 2.004, suggesting the abundant presence of oxygen vacancies in V_O-rich In_2O_3. The electronic configuration of In_2O_3 nanostructures with high V_O material was considerably changed by V_O development. The V_O in the In_2O_3 sample had smaller bandgap energy, and an upshift was seen in the VB tip, according to DRS (Diffuse reflectance spectroscopy) and XPS analysis. Density functional theory (DFT) showed valence band maxima caused a significant DOS. V_O-rich In_2O_3 nanostructures were shown to be more prevalent than V_O-poor In_2O_3 nanostructures, according to a novel concentration of defects. The consequence was a greater carrier level and stronger electric field in the V_O of In_2O_3. The irradiation further energized the electrons in CB. As a result, for H_2O oxidation, V_O-rich In_2O_3 nanostructures performed better than V_O-weak In_2O_3 nanostructures and bulk In_2O_3 by 2.5 and 15 times, respectively. These results confirmed anion vacancy's effectiveness in electrical configuration engineering.

2.2. Cation Vacancies

The cation vacancies, similar to anion vacancies, have a controlling influence headed for electronic, physical, and chemical characteristics of metallic compounds, resulting in various electronic and orbital arrangements [54]. Metal cation vacancies are additionally challenging for the design and management of vacancies because of their superior energy growth, making them complicated to determine their function [48]. Numerous photocatalytic materials with cation vacancies have been developed, and researchers are now examining how they may affect the effectiveness of the photocatalysts [55–57]. The structure-activity connection may be thoroughly explained using 2D atomic layers with and without limited cationic vacancies. Furthermore, tuning such associated vacancies is made easy by the little escape energy of 2D materials.

Moreover, Vv engineering reached larger DOs close to the VB edge. Tailored vacancies boosted light harvesting with a high Vv concentration and increased the catalyst's electrical conductivity. Successful charge separation made it possible to prolong the carrier's lifetime (i.e., 74.5 to 143.6 ns). The photocatalytic efficiency of ~398.3 mol g^{-1} h^{-1} for the production of CH_3OH has been attained using Vv. By using a straightforward hydrothermal process and temperature variation, Jiao et al. created thick $ZnIn_2S_4$ unit cells with few or multi Zn vacancies [58]. The AFM measurements suggested that the $ZnIn_2S_4$ produced unit-cell of thick layers in the direction of the c-axis, while the transmission electron microscopy (TEM) pictures showed a sheet-like shape. The Zeta-potentials, EPR, and PAS measurements of examined products' Zn vacancy-rich and poor properties showed that $ZnIn_2S_4$ layers with different Zn vacancy concentrations were effectively generated, offering two appropriate models for exploring the relationship between Zn vacancies and photocatalyst activities. Because of the high Zn vacancies, the $ZnIn_2S_4$ layers had much better excitons separation performance, as evidenced via PL analysis, ultrafast transient absorption, and surface photovoltage.

Along with improved CO_2 adsorption and hydrophilicity, the abundant V_{Zn} also improved light harvesting from the 440 to the near-infrared range. The dispersal of charge was analyzed by DFT, where the determination was focused on charges in space closer to CB's edge. It appears that electrons are stimulated to CB more rapidly because the Zn vacancy raises the charge density of nearby sulfur atoms. According to Song et al., Ti vacancies in single layer $H_{1.07}Ti_{1.73}O_4 \cdot H_2O$ nanosheets result in the creation of many radical O species which engage with water molecules via H_2 bonds to generate surface coordination. Consequently, photocatalytic efficiency toward H_2 production increased by 10.5 times [59].

Further, the $BiVO_4$ unit cell nanostructures have produced varying levels of vanadium vacancies (Vv in Figure 3). Moreover, X-ray fluorescence (XRF) and positron annihilation spectrometry (PAS) were used to quantify the concentration of Vv at an atomic level. For $BiVO_4$, the Vv was trapped for two samples using the shortest life component (~200 ps) confirmed from PAS [60]. Higher Vv levels were indicated for the reasonable positron power period for $BiVO_4$ nanostructures rich in Vv. According to DFT calculations, the presence of Vv may cause an innovative defect level in the bandgap energy of prepared nanostructures, allowing electrons to be stimulated farther into CB.

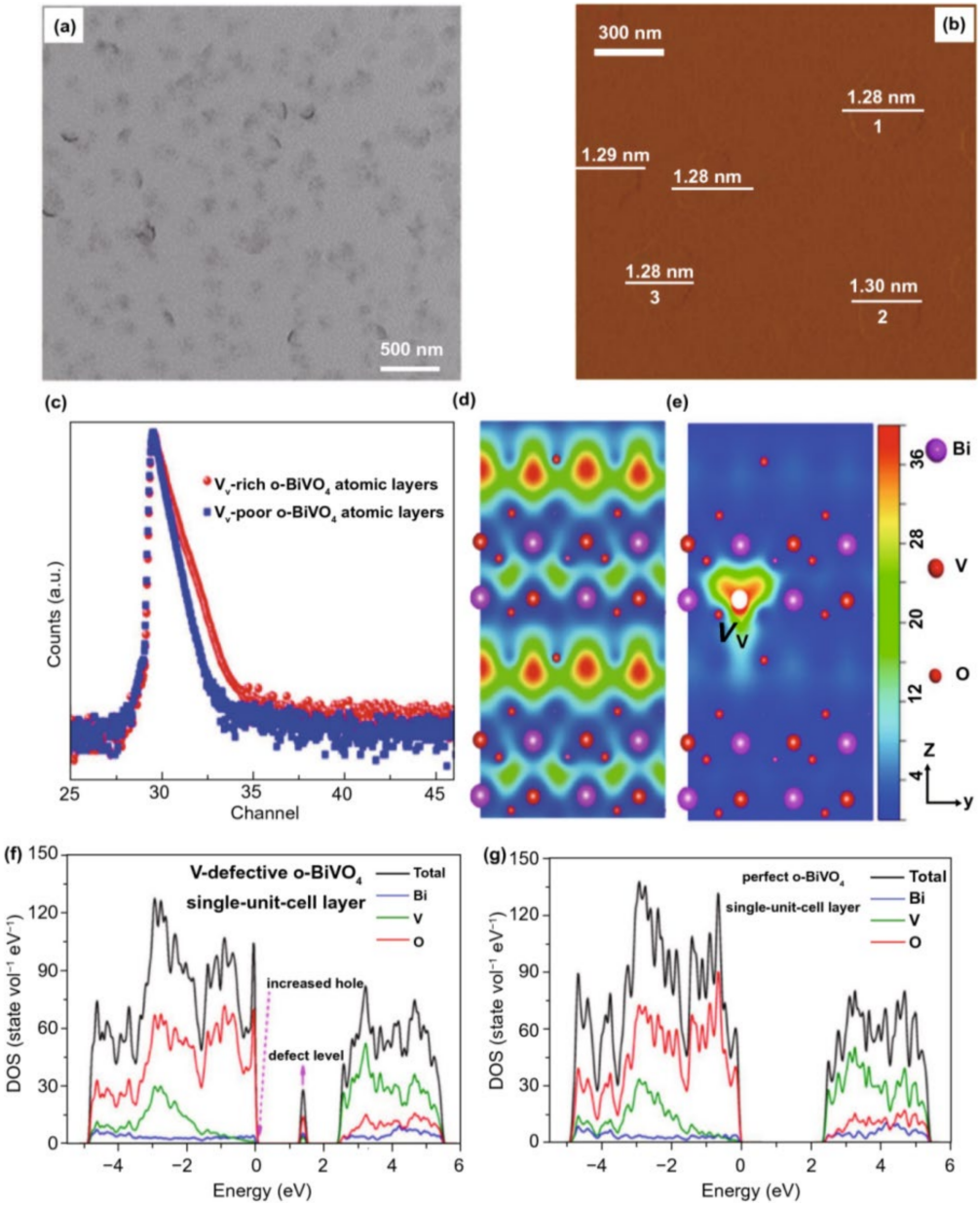

Figure 3. (**a**,**b**) TEM and AFM photographs of V_V-rich o-$BiVO_4$; (**c**–**e**) defects study of Vv-rich and Vv-poor o-$BiVO_4$ atomic layers; (**c**) duration spectra of positron; (**d**,**e**) schematic for entrapped positrons; (**f**) Vv defects in the single unit cell layer slab of o-$BiVO_4$ and slab of pure o-$BiVO_4$ single unit cell estimated by DOSs, (**g**) along [001] direction. Adapted from [60] Copyright 2017, American Chemical Society.

2.3. Other Vacancies Types

The vacancy pairs and voids have been studied to promote the activity of photocatalysts [26,61]. The vacancy pairs usually are formed at the facet with high energy to modulate the local atom structure of photocatalysts, thus improving the photocatalytic activity. For example, the Bi−O vacancy pairs can be formed on the high-energy Bi_2WO_6 (100) facet [62] and serve as a charge separation center (in Bi_2WO_6) to enhance photocatalytic activity [63]. Similar to the role of the Bi−O vacancy pairs in Bi_2WO_6, the Bi−O vacancy pairs in Bi_2MoO_6 also served as a charge separation center, which was reported by Xia et al. [63]. Moreover, these Bi−O vacancy pairs were validated by aberration-corrected scanning transmission electron microscopy in annular dark field mode (STEM-ADF) and positron annihilation spectroscopy, in which dim sites can quickly identify such mixed vacancies.

These Bi−O vacancy pairs contributed to modulating the local atom structure of Bi_2MoO_6, thus improving the CO_2 photoreduction activity. Voids called pits are common volume vacancies in 2D materials. Specifically, when more nearby atoms escape from the lattices, it forms a small region without atoms, which is considered a cluster of vacancies in 2D materials. Vacancy voids are usually formed in ultrathin 2D materials, which is attributed to the escaping of lots of nearby atoms in a small region from the lattices, such as WO_3 [64], BiOCl [65], and C_3N_4 [66] 2D nanomaterials. For instance, Wei et al. [67] reported a three-atomic-layer-thin cerium oxide nanosheet with almost 20% voids occupancy, in which massive pits surrounding cerium sites with average coordination numbers of 4.6 played a vital role in lowering the oxygen activation energy and preventing catalysts poisoning.

3. Environmental Remediation

3.1. Theoretical Insights

Besides the enormous work on lab experiments of 2D photocatalysts and heterojunctions, theoretical studies offered considerable interest. Numerous studies on 2D materials such as CdS/InSe, GeS/WS_2, GeS, $PdSeO_3$, C_2N/WS_2, $Pd_3P_2S_8$, and GeSe have been published in the literature to be effective photocatalysts for photocatalytic reactions variety based on DFT calculations [68–71]. Numerous studies have been conducted to develop a photocatalyst capable of concurrently splitting water into its component in visible light. A $PdSeO_3$ monolayer was proposed as a potential 2D material for complete photocatalytic water splitting based on $PdSeO_3$ layered structure [72]. From DFT calculations, $PdSeO_3$ monolayer cleavage energy (0.42 J m^{-2}) was comparable with graphene (0.37 J m^{-2}), implying a superior probability of attaining $PdSeO_3$ monolayer using the strategy of mechanical exfoliation. According to HSE06 + SOC theory, indirect (2.84 eV) and direct (3.07 eV) bandgap energies for the $PdSeO_3$ monolayer have been assessed, meaning that the $PdSeO_3$ monolayer would effectively harvest light. Additionally, the $PdSeO_3$ monolayer exhibited the best water splitting at a stoichiometric ratio of 2:1 with the help of co-catalysts or sacrificial reagents. The OI sites are supposed to be the active sites for H_2 evolution, whereas the Se sites are anticipated to be the active sites for H_2O oxidation.

Akimove et al. used a hybrid rigid-body MD-extended Hückel theory approach (MD/EHT) to investigate electronic and nuclear dynamics in prolonged systems. Static electronic configuration was also inspected for Ru complexes deposited on the Ta_2O_5 using various anchor groups to determine their photocatalytic CO reduction potential [73]. Calculations revealed that different tilting angles of deposited structures result in a different atmosphere for the catalyst's active site. The horizontal arrangement of the chromophore in the presence of the PO_3H_2 anchor can weaken Ru-CO and Ru-Cl, thus facilitating light-induced reactions by dropping activation energies. The smaller separation between the Ru core and Ta_2O_5 surface is critical if H_2O or CO_2 are partly organized on the substrate subsequent to their reaction involvement.

On the other hand, chromophore vertically coordinated with the COOH group results in tighter Ru-Cl and Ru-CO bonding, significantly reducing the likelihood of reacting species reaching the reaction core. Variations in tilting angle were marginal for Ru complexes attached by an OH anchor, implying extremely small wave function variations and, thus, minute non-adiabatic couplings over time. Conversely, PO_3H_2 exhibited more significant variations, suggesting the possibility of a deeper non-adiabatic coupling between the acceptor and donor states. The performance of various 2D MOs is illustrated in Table 1.

Table 1. Various 2D MOs for environmental remediation with adopted strategies for enhancing the performance.

Application	2D Material	Synthesis	Engineering Tool	Reaction Condition	Performance	Ref.
H_2 evolution	$ZnIn_2S_4$	Solvothermal	Sulfur vacancies	20 vol% TEOA with 3 wt% Pt, Xe lamp (>420 nm)	1504.9 μmol g^{-1} h^{-1}	[74]
	2D $ZnIn_2S_4$/2D g-C_3N_4		Heterojunction	20 vol% TEOA with 3 wt% Pt, Xe lamp (>420 nm)	6095.1 μmol g^{-1} h^{-1}	[74]
	$ZnIn_2S_4$	Hydrothermal	O doping	0.25 M Na_2SO_3 and 0.35 M Na_2S solution, Xe lamp (>420 nm)	2120 μmol $^{-1}$ h^{-1}	[75]
			Pristine sample	0.25 M Na_2SO_3 and 0.35 M Na_2S solution, Xe lamp (>420 nm)	471.11 μmol g^{-1} h^{-1}	[75]
			Monolayer	10 mL TEOA, Xe lamp (>400 nm)	1.723 mmol g^{-1} h^{-1}	[76]
			Bilayer	10 mL TEOA, Xe lamp (>400 nm)	0.799 mmol g^{-1} h^{-1}	[76]
			Monolayer + Sulfur vacancies	10 mL TEOA, Xe lamp (>400 nm)	13.478 mmol g^{-1} h^{-1}	[76]
			Pristine sample	0.25 M Na_2S and 0.25 M Na_2SO_3 solution with 2 wt% Pt, Xe lamp (>420 nm)	263.9 μmol g^{-1} h^{-1}	[77]
	0D $AgIn_5S_8$/2D $ZnIn_2S_4$	Hydrothermal	Heterostructure	0.25 M Na_2S and 0.25 M Na_2SO_3 with 2 wt% Pt, Xe lamp (>420 nm)	949.9 μmol g^{-1} h^{-1}	[77]
CO_2 reduction	TiO_2	Hydrothermal	Pristine sample	A mixture of pure CO_2 gas and H_2O vapor, Xe lamp (>400 nm)	CH_4, 1.643 μmol g^{-1} h^{-1}	[78]
			Surface acidification by H_2SO_4	A mixture of pure CO_2 gas and H_2O vapor, Xe lamp (>400 nm)	CH_4, 1.907 μmol g^{-1} h^{-1}	[78]
		Solvothermal	Pristine sample	100 mL H_2O, Xe lamp	CO, 0.15 μmol g^{-1} h^{-1}	[79]
		In situ ion exchange method	Treated by Lewis base $[WO_4]^{2-}$	100 mL H_2O, Xe lamp	CO, 3.05 μmol g^{-1} h^{-1}	[79]
	WO_3	Solvothermal	Pristine sample	0.2 mL H_2O, silicon nitride lamp (0.8–17 μm)	No product	[80]
			Poor Vo	0.2 mL H_2O, silicon nitride lamp (0.8–17 μm)	CO, 6 μmol g^{-1} h^{-1}	[80]
			Rich Vo	0.2 mL H_2O, silicon nitride lamp (0.8–17 μm)	CO, 2.75 μmol g^{-1} h^{-1}	[80]
	$Sr_2Bi_2Nb_2TiO_{12}$	Solvothermal	Pristine sample	4 M H_2SO_4 with 1.3 g $NaHCO_3$, Xe lamp	CO, 2.62 μmol g^{-1} h^{-1}	[81]
			Rich Vo	4 M H_2SO_4 with 1.3 g $NaHCO_3$, Xe lamp	CO, 17.11 μmol g^{-1} h^{-1}	[81]
	$CuIn_5S_8$	Pristine sample	CO_2 reduction	2 mL H_2O, PLS-SXE 300/300UV Xe lamp (AM 1.5G filter, >420 nm)	CO, 1.3 μmol g^{-1} h^{-1}, CH_4, 1.6 μmol g^{-1} h^{-1}	[82]
		Hydrothermal	Sulfur vacancies	2 mL H_2O, PLS-SXE300/300UV Xe lamp (AM 1.5G filter, >420 nm)	CH_4, 8.7 μmol g^{-1} h^{-1}	[83]
	$ZnIn_2S_4$	Hydrothermal	Zn vacancies	2 mL H_2O, PLS-SXE300/300UV Xe lamp (AM 1.5G filter)	CO, 33.2 μmol g^{-1} h^{-1}	[58]
			Pristine sample	2 mL H_2O, PLS-SXE300/300UV Xe lamp (AM 1.5G filter)	CO, 9.22 μmol g^{-1} h^{-1}	[58]

3.2. H_2O Oxidation

Photocatalytic water splitting was already observed as a potentially game-changing strategy for producing safe and renewable H_2. Hydrogen, with the highest calorific value and the highest energy content by weight, has been identified as a possible energy carrier for storing energy from the sun in chemical bond energy between two H atoms. Due to the slow dynamics of the four-hole half-reaction mechanism in water oxidation, it was critical for optimum splitting performance. As a result, increasing the efficiencies for light-derived H_2O oxidation application by reasonable photocatalyst structure design is highly desirable. In order to design vis-light active semiconductors for H_2O splitting, the E_g (bandgap energy) and band positions must be optimized, charge separation must be adequate, charge movement must be easy, and the semiconductor must be durable in aqueous solutions. The 2D architecture with a high defect density may represent an ideal structure for increasing O_2 generation activity.

The photocatalytic separation of water into its components is observed as the Holy Grail of chemistry because it requires merely a renewable energy source, photocatalysts as a medium, and H_2O as a reaction source. Although a significant move forward has been made, the efficacy of water splitting is quite restricted in the mainstream photocatalytic approaches. Generally, water oxidation is recognized as a slow and inefficient route toward photocatalytic water-splitting schemes because of the complex four-holes redox method. As a result, it is critical to propose a photocatalyst with a robust solar H_2O oxidation system. Additionally, an appealing design strategy for meeting these criteria is combining defective 2D materials such as MoS_2, graphene, and g-C_3N_4 with suitable semiconductors. Because of this, Di et al. engineered rational pit defects in 2D BiOCl nanostructures by partially digging pits on previously prepared BiOCl nanosheets with ethylene glycol [65]. TEM and STEM images clearly showed the engineered pit defects on the (001) exposed facet (Figure 4).

According to DFT calculations, photogenerated electrons gravitate toward the (001) facet in BiOCl, while hs^+ (holes) migrate in the (110) direction. Since O_2 production is a complete hole participating reaction, this appears on the (110) facet via hs^+ extensive migration track to the (110) facet, which eventually includes significant electron–hole recombination. Furthermore, the incorporated pit defects reduced the migration distance of hs^+, thus increasing hs^+ utilization. According to the DFT measurement, the engineered pit defects often marginally improve DOS at CB and VB edges, thus raising carrier concentration and facilitating electron excitation. Additionally, the abundance of unsatisfied chemical bonds accompanying defects created a favorable chemical atmosphere for reaction molecules to chemisorb and foster photocatalytic water oxidation reactions. Therefore, the pit-rich BiOCl-nanosheet could generate O_2 at 56.85 mol g^{-1} h^{-1}, between three and eight times faster than the BiOCl-nanosheet and bulk BiOCl. In another study, ultrasonic exfoliation of lamellar hybrid intermediate (Zn_2Se_2)(propylamine) resulted in the formation of four atomic thin freestanding single-layers ZnSe [84]. Although the size of ZnSe had been atomically reduced, the local atomic structure had undergone remarkable improvements. Simultaneously, the bond lengths for Se–Se was improved from 4.012 to 4.11. These findings established surface distortion in single-layer structures, which resulted in decreased surface energy and exemplary stability of fabricated structures in single-layers.

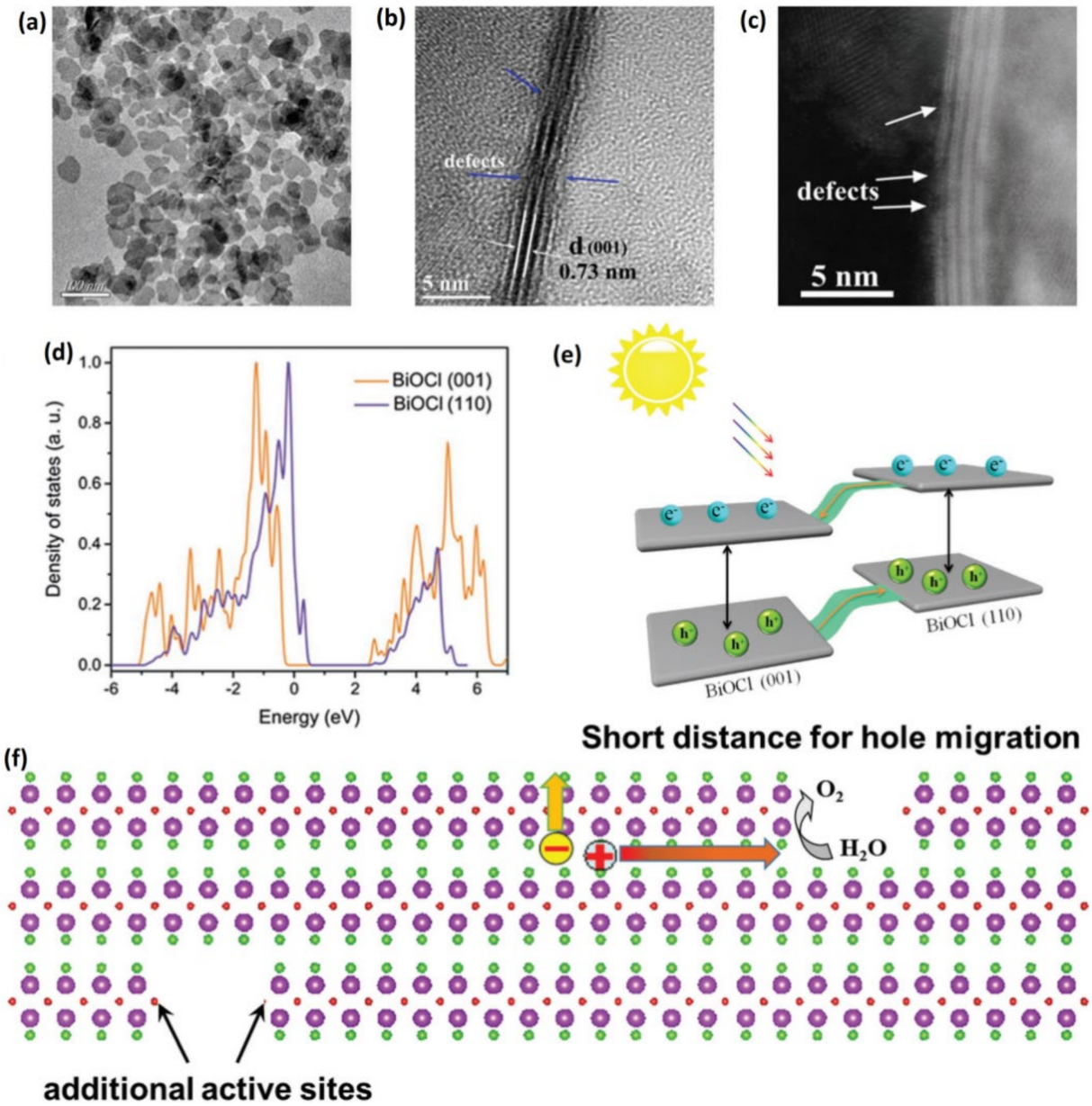

Figure 4. (**a**,**b**) TEM photograph and (**c**) HAADF-STEM images BiOCl nanosheets with defects; (**d**) DOS diagrams of BiOCl (001) and (110) faces from first-principles simulations; (**e**) charge migration between 001 and 110 facets is shown in this diagram; (**f**) photogenerated charges are separated and transferred in this schematic illustration. Adapted from [65] Copyright 2017, The Royal Society of Chemistry.

Additionally, surface deformation can increase DOS at the CB tip, ensuring an even higher charge carrier transfer rate. The ZnSe single layer exhibit high light-harvesting, improved exciton separation, and lower resistance to charge carriers due to their single-layer configuration with surface defects. As a result, single layers ZnSe nanostructures demonstrated a 195-fold increase in photocatalytic efficiency for H_2O oxidation following Xe lamp irradiation relative to bulk ZnSe. Correspondingly, defects engineered in other 2D photocatalysts, including V_Os confined in In_2O_3; pits formed in WO_3 nanosheet; or surface distortions formed in ZnSe, SnS_2, and SnS nanosheet, will show superior photocatalytic water oxidation behaviors [52,64,85]. Liu et al. developed a variety of pore structures in WO_3 nanostructures using a rapid heating technique on previously exfoliated $WO_3 \bullet 2H_2O$-nanostructures [86]. Given the photogenerated hs^+ migration direction was along 001 facets

in the x-direction in W-O-W chains, the photogenerated hs^+ almost certainly experienced many charge carrier recombination, severely impairing photocatalytic efficiency. The pores formed effectively shorten the diffusion path of hs^+ and promote H_2O oxidation to form O_2 at the WO_3 surface. Additionally, an abundance of dangling bonds along the pore environment provided favorable conditions for facile chemisorption of molecular reactions, which increased O_2 evolution kinetics. Photocatalytic H_2O oxidation efficiency was increased by 18 times when pore-rich WO_3. Moreover, ultrathin nanostructures were compared to bulk WO_3. It demonstrates an important technique for increasing conversion efficiency with a 2D structure for photocatalytic H_2O oxidation.

3.3. H_2 Evolution

Although photocatalytic sunlight conversion to H_2 fuels is an optimal choice for achieving sustainable energy in the future, its comparatively poor energy conversion performance severely limits its practical applications. Numerous remarkable catalytic materials have been used in photocatalytic H_2 production; however, the majority are still said to have very low photocatalytic efficiency, which cannot satisfy the requirements of practical industrial applications. The photocatalytic H_2 processing efficiency can be significantly increased by combining a 2D structure with abundant surface defects [87].

3.3.1. Mechanism

The nanomaterials' composition, atomic arrangement, and morphology play a key aspect. The electron−hole pairs are yielded when the laser's energy is greater than their bandgaps [88,89]. The photogenerated charges within the nanomaterials react with adsorbed H_2O on the surface. However, the charge carriers also undergo recombination or are trapped at internal defects before reaching the surface. Ida et al. found that both time and energy played two key factors during the water splitting to give hydrogen (Figure 5) [90], which requires $4e^-$ generations. Thus, the surface of nanomaterials has impinged with four photons for a short period (at least 4 ms). The layered structures can aid light absorption and largely shorten the traveling distance of the photogenerated charges to reduce their recombination [88,90]. In 1958, Parsons et al. found that the catalytic H_2 evolution occurred on the catalysts' surface [91]. Moreover, Norskov et al. simulated the activity to understand the efficiency [92]. The water splitting involves two basic reactions (Equations (1)–(3)):

$$2H^+ + 2e^- \rightarrow H_2 \rightarrow E^0 = 0.00\ V \quad (1)$$

$$2H_2O \rightarrow O_2 + 4H^+ + 4e^- \rightarrow E^0 = +1.23\ V \quad (2)$$

$$\text{All:}2H_2O \rightarrow O_2 + 2H_2$$

$$\Delta E^0 = 1.23\ V,\ \Delta G^0 = +237.2\ kJ\ mol^{-1} \quad (3)$$

The water splitting to H_2 by solar energy is one of the most eco-friendly methods. A high H_2 production over photocatalysts of the semiconductor materials can be achieved by sunlight or visible light. It is reliable that the semiconductor can adsorb sufficient energy and results in the creation of electron−hole pairs.

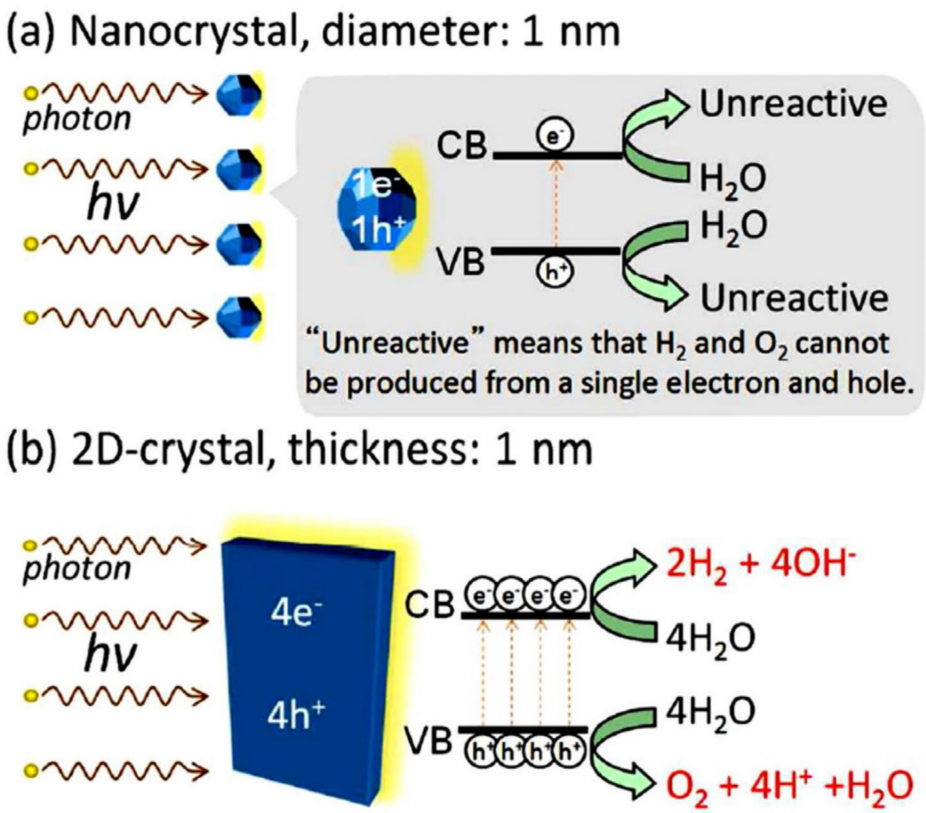

Figure 5. Schematic illustration of the photocatalytic water splitting reaction under solar light illumination for an (**a**) nanocrystal photocatalyst and (**b**) 2D photocatalyst. Adapted from [90] Copyright 2014, American Chemical Society.

3.3.2. Recent Progress

In order to increase the H_2 generation performance, 2D materials with atomic thickness, such as Cu_2O (cubic), were created [93]. AFM analysis revealed ~0.62 nm thickness, which corresponds to the four atomic-level thicknesses of Cu_2O in the [011] direction. Consequently, cubic Cu_2O surface energy was reduced to the order of (111) (100) (110). Since (110) and (011) surfaces are identical facets (011), they also demonstrated high surface energy, which results in a high operation. Due to their significantly decreased thickness, atomically thin Cu_2O-nanostructures had a different electronic composition than bulk equivalents. DFT simulations revealed significantly improved DOSs at the VB edge for prepared nanostructures in contrast to bulk Cu_2O. Simultaneously, expanded CB edge in 2D Cu_2O-nanostructures was investigated in comparison to bulk Cu_2O, demonstrating that atomically thick Cu_2O has high carrier mobility and a minimal E_g. Taking advantage of these benefits, a photocatalytic H_2 evolution rate greater than 36 times that of 2D Cu_2O nanostructures was achieved following visible light irradiation. These findings unequivocally demonstrated that 2D materials might have significant benefits for H_2 evolution and a variety of remarkable activities. By combining the ultrathin structure and V_O, the photocatalytic H_2 production rate of defect-rich $K_4Nb_6O_{17}$ nanosheet can be significantly increased to 1661 mol g^{-1} h^{-1}, approximately 7- and 21-fold of defect-free $K_4Nb_6O_{17}$ nanosheet, respectively [94]. Not only does the surface V_Os close the E_g and increase light absorption, but they also act as charge separation centers, effectively separating photogenerated electron–hole pairs. Apart from facilitating charge isolation, the V_Os offer a bridge between two elements, allowing for the formation of close junctions. Zhang et al. [95] obtained 1T MoS_2 monolayers supported on the end-faces of $Bi_{12}O_{17}Cl_2$ sheet to create a 2D Janus Cl_2-$Bi_{12}O_{17}$-MoS_2 bilayer junctions, which is different from Van der Waals heterostructures (Figure 6a–k). Electrons were separated by the internal electric

field of $Bi_{12}O_{17}$ of visible light $Bi_{12}O_{17}Cl_2$, which migrated to MoS_2 through the Bi–S bonds, and holes were formed at the internal electric field of Cl_2 end-faces. Thus, the Janus bilayers gave a superior photocatalytic hydrogen evolution rate of 33 mmol h^{-1} g^{-1} and a carrier lifetime of 3.446 ps (Figure 6m–o) [95]. In another case, the direct Z-Scheme photocatalyst 2D/2D Fe_2O_3/g-C_3N_4 generates H_2 almost 13 times compared to g-C_3N_4 [96]. With the variance of work functions among Fe_2O_3 (4.34 eV) and g-C_3N_4 (4.18 eV), the switching of electrons will occur from g-C_3N_4 to Fe_2O_3 at an intimate 2D/2D interface. Thus, at the Fe_2O_3/g-C_3N_4 interface, a built-in electric field is created, which becomes advantageous for photoinduced charge carrier transfer and separation. Additionally, a direct Z-scheme system that relies on the band structures of Fe_2O_3 and g-C_3N_4 has been established. After all, electrons formed in the CB of Fe_2O_3 will pass through the intimate 2D/2D interface to the VB of g-C_3N_4 and afterward recombine with the hs^+ through d-p conjugation, hence impeding photogenerated charge carrier recombination. As an effect, photoinduced electrons and holes accumulate in g-C_3N_4 at CB and Fe_2O_3 (VB), respectively. Not only will this direct Z-scheme method increase exciton separation performance, but it also generates a major driving force for the light-driven splitting of water, thus increasing the ability of g-C_3N_4.

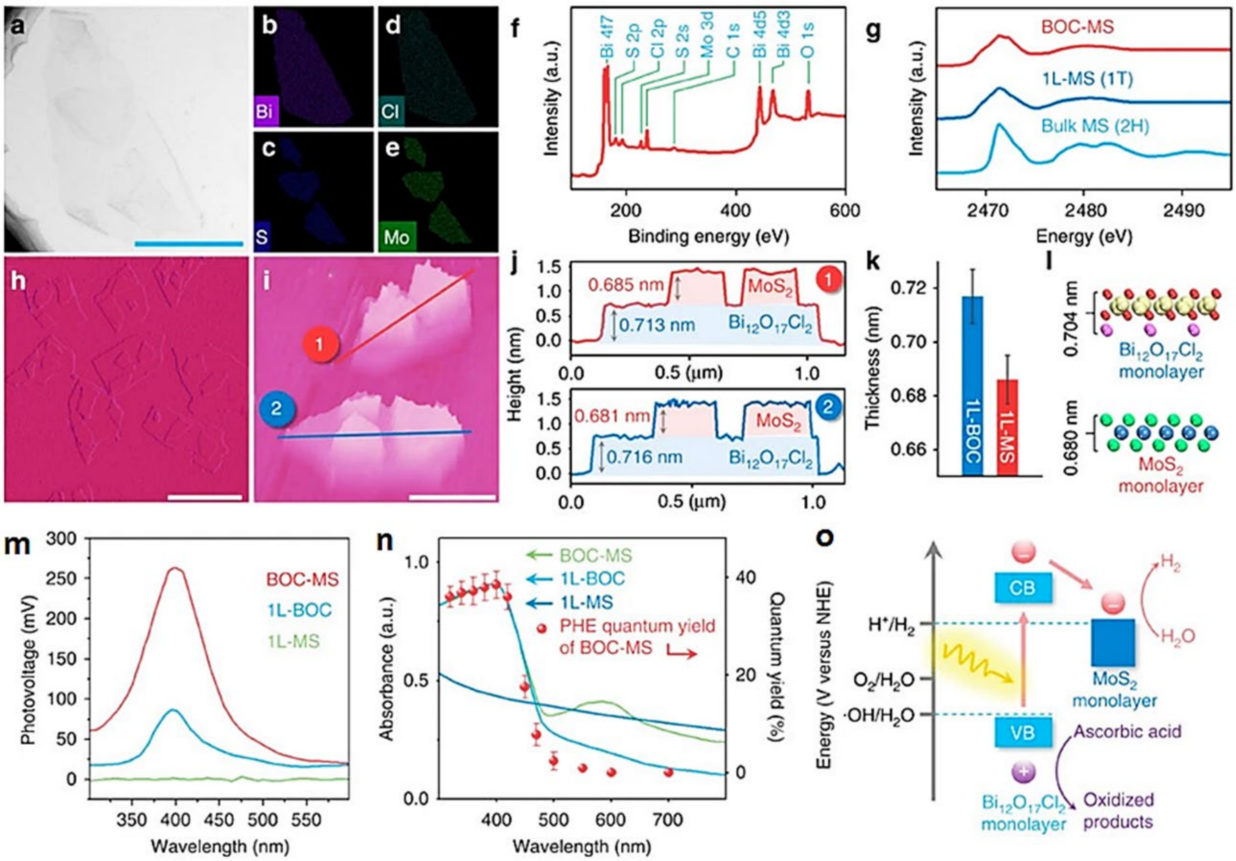

Figure 6. (**a**) Top-view TEM image; (**b**–**e**) elemental mapping images; (**f**) XPS spectra; (**g**) S K-edge X-ray absorption near edge structure spectra of $Bi_{12}O_{17}C_{l2}$-MoS_2, 1L-MoS_2 and bulk MoS_2; (**h**,**i**) AFM images; (**j**) height profiles along the lines in I; (**k**) comparison of the average thicknesses of 1L-$Bi_{12}O_{17}C_{l2}$ and 1L-MoS_2 in $Bi_{12}O_{17}C_{l2}$-MoS_2 monolayers; (**l**) the theoretical thicknesses of MoS_2 and $Bi_{12}O_{17}C_{l2}$ monolayers; (**m**) surface photovoltage spectroscopy of 1L-$Bi_{12}O_{17}C_{l2}$, 1L-MoS_2 and $Bi_{12}O_{17}C_{l2}$-MoS_2; (**n**) UV-visible diffuse reflectance spectrum of $Bi_{12}O_{17}C_{l2}$-MoS_2, 1L-$Bi_{12}O_{17}C_{l2}$ and 1L-MoS_2, and photocatalytic hydrogen evolution quantum yields of $Bi_{12}O_{17}C_{l2}$-MoS_2 monolayers plotted as a function of wavelength of the incident light; (**o**) band alignments in 1L- $Bi_{12}O_{17}C_{l2}$ and 1L-MoS_2. Adapted from [95] Copyright 2016 Springer Nature Limited.

3.4. CO_2 Reduction

Over the past century, fossil fuel burning has raised CO_2 levels in the atmosphere, leading to widespread climate change. By using an effective photocatalyst, conversions of CO_2 to chemicals such as CO, CH_4, CH_3OH, HCOOH, and HCHO is a feasible approach to mitigate greenhouse influence and discourse the energy crisis [97,98]. However, the activation of CO_2 is challenging since the C-O bond has higher dissociation energy (750 kJ mol^{-1}) and requires several electrons. Further, the development of CO_2-intermediate via single e^- transmission was recognized in the reduction strategy as a rate-limiting path.

3.4.1. Mechanism

The CO_2 photoreduction is the energy conversion process involving three main steps: (i) absorbing photons and generating charge carriers; (ii) separating photogenerated carriers and transferring them from the interior to the photocatalyst surface; and (iii) reducing the CO_2 into value-added fuels and chemicals by photogenerated electrons [99,100]. Then the final products will be desorbed from the catalyst surface to facilitate the subsequent reaction. Note that the CO_2 reduction with H_2O is a very complicated reaction involving two mechanisms: (i) the $1e^-$ transfer process and (ii) the multiple proton-coupled e^- transfer process. In Figure 7A and mechanism I, the single electron can activate CO_2, forming $CO_2{}^{*-}$ intermediate [101], which requires a potential of −1.9 V versus NHE (normal hydrogen electrode). Thus, this process is thermodynamically unfavorable and is a large recombination energy between the linear CO_2 and the $CO_2{}^{*-}$ intermediate. In mechanism II, the route bypasses the $CO_2{}^{*-}$ formation [102], and different products are yielded, e.g., CO, HCOOH, HCHO, CH_3OH, CH_4, and multi-carbon products (e.g., CH_3CH_2OH, C_2H_6, and C_2H_4), Table 2. In addition to the supply of electrons and protons, The C–C coupling needs more supply of electrons and protons, restricting yield and selectivity. Thus, stable intermediates should have participated in C–C couplings [103,104].

Table 2. Possible products of CO_2 and water reduction with corresponding reduction potential (versus NHE at pH 7 in aqueous solution). Adapted from [106–108] Copyright 2019, Elsevier; 2020 The Royal Society of Chemistry; 2019, American Chemical Society.

Product	Reaction	E^0 (V vs. NHE)
Hydrogen	$2H_2O + 2e^- \rightarrow 2OH^- + H_2$	−0.41 V
Carbon monoxide	$CO_2 + 2H^+ + 2e^- \rightarrow CO + H_2O$	−0.51 V
Formic acid	$CO_2 + 2H^+ + 2e^- \rightarrow HCOOH$	−0.58 V
Oxalic acid	$2CO_2 + 2H^+ + 2e^- \rightarrow H_2C_2O_4$	−0.87 V
Methanol	$CO_2 + 6H^+ + 6e^- \rightarrow CH_3OH + H_2O$	−0.39 V
Methane	$CO_2 + 8H^+ + 8e^- \rightarrow CH_4 + 2H_2O$	−0.24 V
Ethanol	$2CO_2 + 12H^+ + 12e^- \rightarrow C_2H_5OH + 3H_2O$	−0.33 V
Ethane	$2CO_2 + 14H^+ + 14e^- \rightarrow C_2H_6 + 4H_2O$	−0.27 V

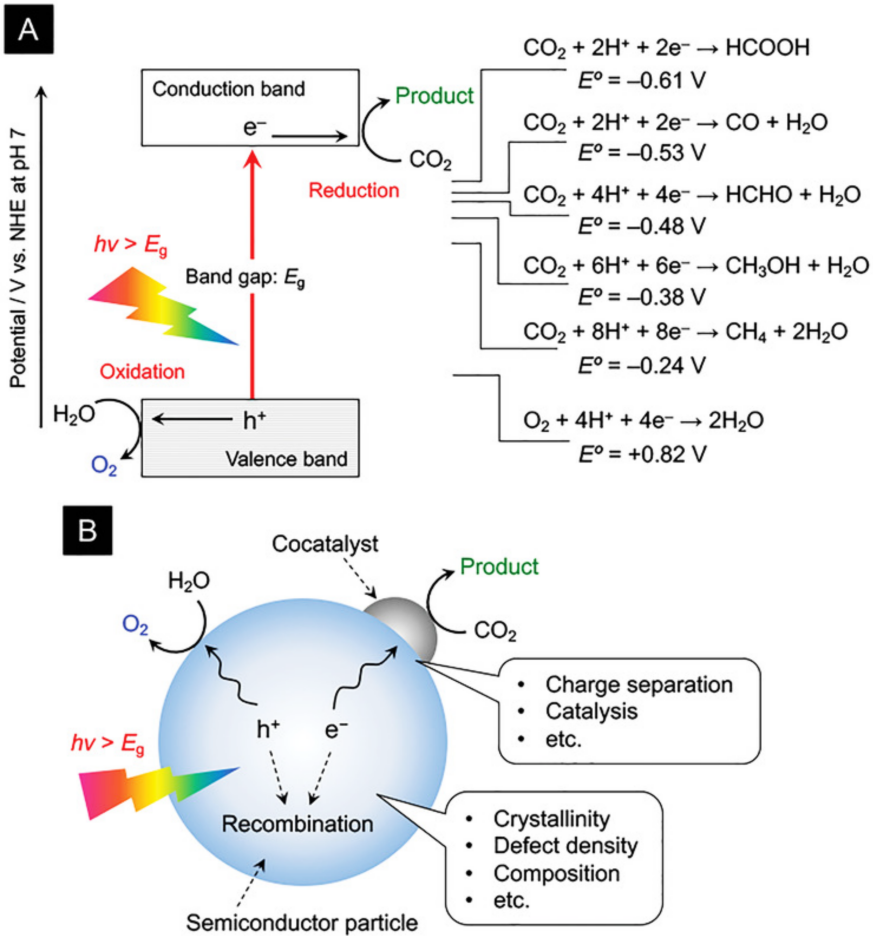

Figure 7. (**A**) Schematic energy diagram for CO_2 reduction and (**B**) H_2O oxidation over 2D photocatalysts. Adapted from [105] Copyright 2019 Wiley.

Notably, the mechanism is different when CO_2 is reduced by CH_4 and H_2 (Table 3) [109]. Two pathways involve in the CO_2 conversion to CO: (i) H_2 only acts as the reducing agent and does not participate in the intermediate formation; (ii) formate is the intermediate [110]. The CO_2 conversion with H_2 to CH_4 is called a Sabatier reaction, where CO is the intermediate determining two different reduction pathways. The mechanism of CO_2 reduction to CH_3OH is similar to CO_2 methanation [111]; CO_2 is converted to CO, then the CO is formed into CH_3OH. Note that the whole process can occur without the CO's participation.

Table 3. The reaction process in which CO_2 is reduced by H_2 and CH_4 and the required ΔH_{298K} (kJ mol^{-1}). Adapted from [112] Copyright 2016 Royal Society of Chemistry.

Reaction	ΔH_{298K} (kJ mol^{-1})
$CO_2 + H_2 \rightarrow CO + H_2O$	41.2
$CO_2 + 4H_2 \rightarrow CH_4 + 2H_2O$	−252.9
$CO_2 + 3H_2 \rightarrow CH_3OH + H_2O$	−49.5
$CO_2 + CH_4 \rightarrow 2CO + 2H_2$	247

The CO_2 reduction to valuable chemicals with high yield and selectivity of product is still a big challenge. Firstly, the CO_2 molecule is highly stable due to its high dissociation energy of C=O (>750 kJ mol^{-1}). Thus, it requires significant energy input. Secondly, HER may compete when water is present as a reducing agent, which consumes H^+ and electrons to produce H_2, and CO_2 is low solubility in water, so water reduction prefers to occur.

Thirdly, various products can be generated during CO_2 reduction. Thermodynamically, methanol and methane tend to be formed due to less potential energy required. Regarding kinetics, CO and formic acid are easily formed due to the lower number of electrons required [113–115]. Thus, some conditions should be satisfied to enhance the CO_2 reduction: (i) photocatalysts should have an appropriate band structure; (ii) the band position matches well with the potential required for CO_2 reduction. The CB edge potential should be lower than the potential for CO_2 reduction, and the VB edge potential should be higher than the oxidation potential of the reducing agent. Additionally, the bandgap (the ideal one is 1.75–3.0 eV) should be close to the potential required for CO_2 reductions [116]. Furthermore, the efficient CO_2 adsorption on the surface is the basis for excellent photocatalytic activity; the adsorbed CO_2 and photogenerated electrons combine quickly to yield products.

3.4.2. Recent Progress

A theoretical potential of −1.9 V vs. NHE is required for initialization, and a higher overpotential is desired for exploited potentials. In 1979, Inoue et al. found the photoconversion of CO_2, and numerous photocatalysts have been well developed [102]. Due to the strong thermodynamic strength of CO_2 (G = −394.4 kJ mol^{-1}), the CO_2 activation to reactive intermediates on the surface of photocatalysts is a significant concern [117]. Thus, CO_2 adsorption and activation are critical for photocatalytic CO_2 conversions. Defective 2D photocatalysts exhibit exceptional CO_2 photoreduction activity. For instance, by reducing ultrathin ZnAl-LDH, V_O defects were created [50]. The ZnVO complexes acted as traps for CO_2 and H_2O molecules, promoting charge separation and enhancing CO_2 photoreduction activity to give CO. The presence of anion and cation vacancies can promote photocatalytic CO_2 reduction. A lamellar hybrid intermediate approach has been applied to prepare Bi_2WO_6 layers [118]. Sodium oleate was used to bind with Bi^{3+}, forming lamellar Bi oleate complexes by self-assembling oleate ions in a head-to-head or tail-to-tail bilayer sequence to form a mesostructure. As Na_2WO_4 was injected and hydrothermally refined, whereas self-exfoliation was subjected to Bi_2WO_6 developed into a single-unit cell sheet, which is used for CO_2 photoreduction. Moreover, the constant bubbling of incredibly pure CO_2 gas was acquired in an aqueous solution. An average rate of 75 mol_{CH_3OH} g^{-1} h^{-1} was observed over Bi_2WO_6 layers over a 5 h period, which is ~3 and 0.5 times faster than Bi_2WO_6 nanocrystals and bulk Bi_2WO_6, respectively. Engineered Zn vacancies into $ZnIn_2S_4$ increased charge separation efficiency [58], resulting in a CO formation rate of 33.2 mol g^{-1} h^{-1}, which was ~3.6-fold of Zn vacancy-deficient $ZnIn_2S_4$. In a 2D/2D g-C_3N_4/NiAl-LDH hybrid heterojunction [119], the negatively charged g-C_3N_4 acted as nucleation sites for the in situ growth of NiAl-LDH, giving an intimate interface. The g-C_3N_4/NiAl-LDH exhibited a significantly higher CO conversion rate of 8.2 mol h^{-1} g^{-1} than pure g-C_3N_4 and NiAl-LDH. Moreover, the selectivity toward CO is ~82%. In addition, the g-C_3N_4/NiAl-LDH improved CO generation and the evolution of H_2 and O_2. Further, Xie et al. found that o-$BiVO_4$ layers with V vacancies in the forbidden band with a higher Fermi-level h^+ density displayed a high rate of CH_3OH formation [60]. The V_V-rich o-$BiVO_4$ layers can enhance light absorption and carrier separation with a carrier lifetime of 143.6 ns. A CH_3OH formation rate was up to 398.3 mol g^{-1} h^{-1}, which is ~1.4-fold of the V_V-deficient o-$BiVO_4$. The V_V-rich o-$BiVO_4$ layers also displayed outstanding cycling resistance for a 96 h reaction. Tonda et al. [120] reported a 2D/2D/2D heterojunction of Bi_2WO_6, reduced graphene oxide, and g-C_3N_4 (BWO/RGO/CN) for efficient photoreductions. Of note, RGO here acted as a capturer of the electrons from CN and as a redox mediator to improve the charge transfer between BWO and CN. The BWO/RGO/CN with 1 wt% RGO and 15 wt% BWO showed enhanced activity towards the reduction in CO_2 to yield CH_4 and CO using visible-light, compared to the P25 and other synthesized catalysts. BWO/RGO/CN achieved a H_2 selectivity of 92%. It was attributed to the 2D/2D/2D structure with large interfacial contact, which is favor to the rapid charge transfer and the hindering of the recombination of photoinduced electrons and holes.

The improvement of CO_2 adsorption also is critical to enhancing photocatalytic efficiency. As Ti_3C_2 MXene has good electrical conductivity and exposed metal sites, ultrathin Ti_3C_2/Bi_2WO_6 was obtained [121], exhibiting a strong interface between Ti_3C_2 and Bi_2WO_6. The –O or OH group on the Ti_3C_2 surface aids in capturing photoinduced e^- from Bi_2WO_6. Since Bi_2WO_6's CB potential exceeds Ti_3C_2's Fermi stage, the photoinduced e^- passes from Bi_2WO_6 to Ti_3C_2. Ti_3C_2/Bi_2WO_6-nanosheet pores with increased specific surface area promoted CO_2 adsorption, which reacts to CH_4 and CH_3OH with photoinduced e^-. Of note, O_2 can be converted to an H_2O by-product in the photocatalytic CO_2 conversion (Figure 8a). The alkalinization of co-catalyst (Ti_3C_2 MXene) with P25 was applied by Ye et al., which stemmed in a substantial development in photocatalytic CO_2RR [122]. The 5% $Ti_3C_2(OH)_2$ doped P25 (TC-OH/P25) shows significant outcomes towards CH_4 release than unmodified TC/P25 (Figure 8b). Accordingly, DFT investigations revealed that CO_2 adsorption energy on TCF (F termination) exceeded that of TC-OH (OH termination). As a response, CO_2 molecules are adsorbed onto TC-OH, forming activated CO_3^{2-}. Facilitating activation sites, charging isolation, sufficient CO_2 adsorption, and outstanding electrical conductance of alkalinized MXene resulted in significant photocatalytic progress.

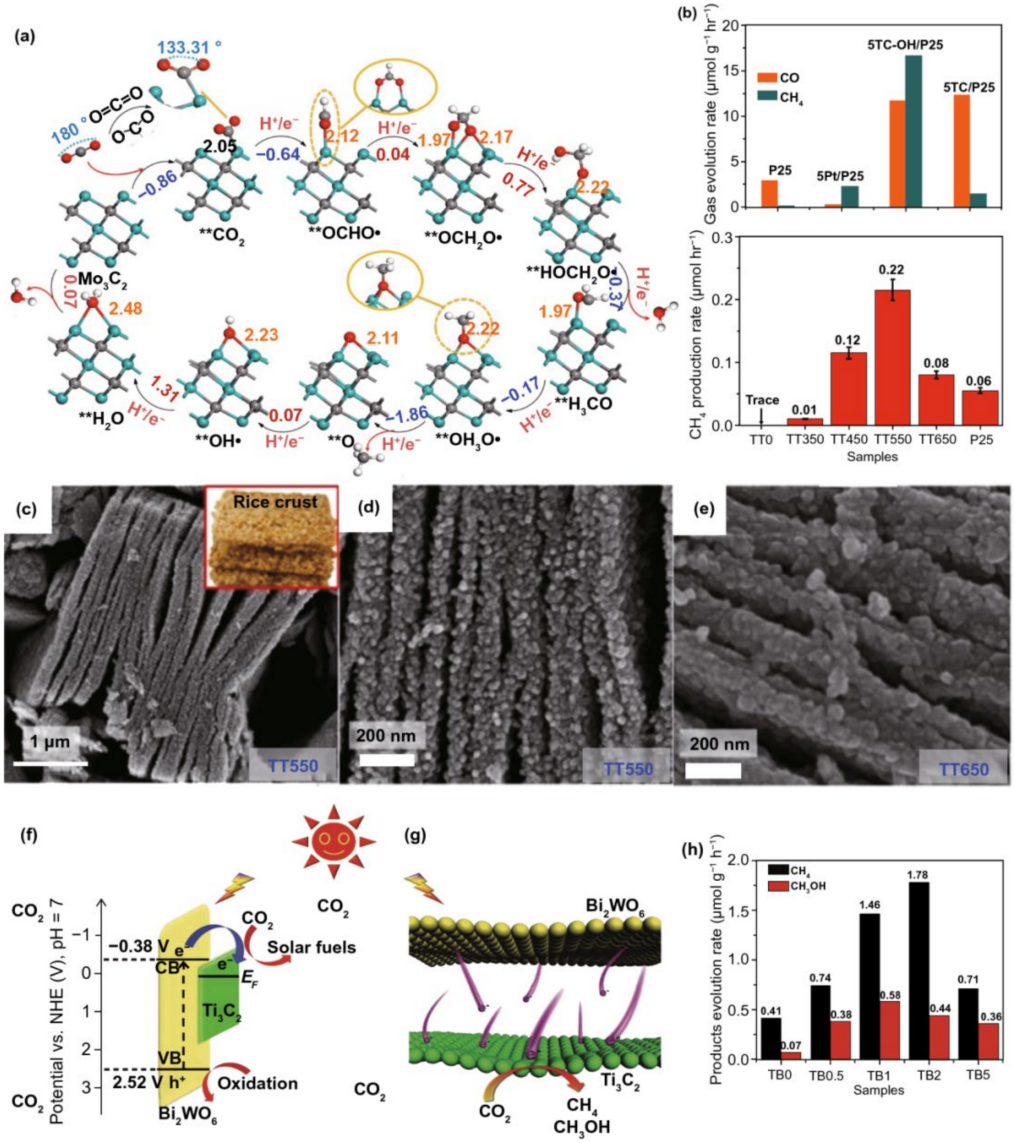

Figure 8. (**a**) For CO_2 to *CH_4 and **H_2O conversion, the lowest amount of energy paths were explored, catalyzed by Mo_3C_2. Adapted from [123] Copyright 2017, American Chemical Society. (**b**) CO and CH_4

evolution rates photocatalytically over P25, Pt/P25, TC/P25, and TCOH/P25. Adapted from [124] Copyright 2016, American Chemical Society. (**c**–**f**) P25 for CH_4 generation and photocatalytic CO_2RR of TiO_2/Ti_3C_2 (TT-x) samples (**c**) and images of TT550 obtained with FESEM. Adapted from [49] Copyright 2015, American Chemical Society. (**g**) Photoinduced e^- migration technique at Ti_3C_2/Bi_2WO_6 heterointerface and (**h**) photocatalytic activity of Ti_3C_2/Bi_2WO_6. Adapted from [121] Copyright 2018, Wiley.

Xu et al. [125] reported TiO_2/Ti_3C_2 composites for CO_2RR to generate CH_4 (Figure 6c). The rice crust morphology of TT550 and TT650 was observed to differ from Ti_3C_2 (Figure 8d–f). The e^- is efficiently transferred to TiO_2, and the unique morphology provides abundant active sites to enhance photocatalytic performance. However, evaluating $TiO_2/Ti_3C_2T_x$ systems was difficult because of the different morphology and surface modification by MXene, and TiO_2 phases. They recently fabricated an ultrathin heterojunction of Ti_3C_2/Bi_2WO_6 (Figure 8g). The separation and transport of photogenic charges were improved due to intensive electronic coupling and physical effects. Ti_3C_2 (2%)/Bi_2WO_6 showed the highest CH_4 release rate (Figure 8h). Moreover, the large interfacial contact area of 2D/2D heterojunction offered shortened diffusion lengths at the interfaces, generating superior charge mobility in contrast to 1D/2D and 0D/2D ones. These 2D/2D heterojunctions have engendered a new potential in photocatalytic CO_2RR.

4. Conclusions and Perspective

Engineered 2D materials are excellent for elementary photocatalytic processing and have many possible commercial uses. This review focuses on significant progress in applying 2D materials for photocatalytic solar conversion. Different surface defect forms, for instance, anion-cation vacancies, have been used to adjust the microstructure, atom coordination number, electronic structure, carrier concentration, or electrical conductivity of 2D MOs, thereby improving photocatalytic efficiency. The current study summarizes defect engineering, including anion and cation vacancy creation and several photocatalytic applications (water splitting, HER, and CO_2RR).

Despite rapid development in 2D MOs for photocatalysis, this field faces many obstacles. Apart from the recent advances outlined here, research in this field is still in its infancy; issues and challenges in the proposal, synthesis, and application of defective 2D MOs remain. Though various top-down and bottom-up approaches were used to synthesize 2D materials beyond graphene, large-scale preparation of 2D materials remains difficult. The mass development with specified surface defects would be critical for photocatalytic applications. In order to investigate diverse and abundant synthetic strategies for defect-rich 2D MOs with an atomic-scale thickness on a large scale are additionally assorted, and plentiful synthesis approaches should be investigated.

A variety of 2D materials, particularly those with a defect-rich design, would be unstable physicochemically. In the course of the store, along with photoreaction procedures, isolated nanosheets can endure irreversible aggregation and structural disintegration, resulting in the loss of advanced structural characteristics. Moreover, along with surface Vos, certain faults would be filled by ambient H_2O or O_2 during long-term photocatalytic action, negating the microenvironment's distinct benefits.

Photocatalysts based on 2D MOs can be critical in solving the environmental and energy problems associated with photochemical conversion aided by sunlight. Furthermore, most photocatalytic activity is still in the manual trial-and-error stage, with many of the reaction mechanisms unclear. Certain underdeveloped, highly efficient 2D photocatalysts can be ignored due to the restricted preparation processes. With the introduction of machine learning and DFT computing, increased emphasis must be placed on developing more stable and efficient 2D materials and heterojunctions in two dimensions.

Likewise, environmental considerations about the solar-powered 2D device are essential for commercial applications. However, no research is being conducted on this subject at the moment. Biocompatibility evidence for 2D components used in biomedical applications may be used to approximate their environmental impact. While stable 2D binary

compounds such as MoS_2 and MXenes are nontoxic, unstable MXenes such as tellurene are harmful. Further investigation of the 2D material's long-term environmental impact is recommended.

Author Contributions: Investigation, A.R. and Y.Z.; resources, Y.Z. and A.R.; writing—original draft preparation, G.L., Y.Z. and A.R.; writing—review and editing, A.C. and G.L.; supervision, A.C. and G.L.; project administration, G.L. All authors have read and agreed to the published version of the manuscript.

Funding: This research received no external funding.

Institutional Review Board Statement: The study was conducted in accordance with the Declaration of Helsinki and approved by the Institutional Review Board.

Conflicts of Interest: The authors declare no conflict of interest.

References

1. Di, J.; Xiong, J.; Li, H.; Liu, Z. Ultrathin 2D Photocatalysts: Electronic-Structure Tailoring, Hybridization, and Applications. *Adv. Mater.* **2018**, *30*, 1704548. [CrossRef] [PubMed]
2. Qamar, S.; Lei, F.; Liang, L.; Gao, S.; Liu, K.; Sun, Y.; Ni, W.; Xie, Y. Ultrathin TiO_2 flakes optimizing solar light driven CO_2 reduction. *Nano Energy* **2016**, *26*, 692–698. [CrossRef]
3. Gao, S.; Lin, Y.; Jiao, X.; Sun, Y.; Luo, Q.; Zhang, W.; Li, D.; Yang, J.; Xie, Y. Partially oxidized atomic cobalt layers for carbon dioxide electroreduction to liquid fuel. *Nature* **2016**, *529*, 68–71. [CrossRef] [PubMed]
4. Gao, S.; Sun, Y.; Lei, F.; Liu, J.; Liang, L.; Li, T.; Pan, B.; Zhou, J.; Xie, Y. Freestanding atomically-thin cuprous oxide sheets for improved visible-light photoelectrochemical water splitting. *Nano Energy* **2014**, *8*, 205–213. [CrossRef]
5. Luo, B.; Liu, G.; Wang, L. Recent advances in 2D materials for photocatalysis. *Nanoscale* **2016**, *8*, 6904–6920. [CrossRef]
6. Qin, Z.; Hu, S.; Han, W.; Li, Z.; Xu, W.; Zhang, J.; Li, G. Tailoring optical and photocatalytic properties by single-Ag-atom exchange in $Au_{13}Ag_{12}(PPh_3)_{10}Cl_8$ nanoclusters. *Nano Res.* **2022**, *15*, 2971–2976. [CrossRef]
7. Shi, Q.; Qin, Z.; Waheed, A.; Gao, Y.; Xu, H.; Abroshan, H.; Li, G. Oxygen Vacancy Engineering: An Approach to Promote Photocatalytic Conversion of Methanol to Methyl Formate over CuO/TiO_2-Spindle. *Nano Res.* **2020**, *13*, 939–946. [CrossRef]
8. Wang, L.; Sasaki, T. Titanium Oxide Nanosheets: Graphene Analogues with Versatile Functionalities. *Chem. Rev.* **2014**, *114*, 9455–9486. [CrossRef]
9. Raoufi, D. Transparent thin films of pure anatase Titania nanoparticles with low surface roughness prepared by electron beam deposition method. *Mater. Res. Express* **2019**, *6*, 096406. [CrossRef]
10. Balendhran, S.; Walia, S.; Nili, H.; Ou, J.Z.; Zhuiykov, S.; Kaner, R.B.; Sriram, S.; Bhaskaran, M.; Kalantar-zadeh, K. Two-Dimensional Molybdenum Trioxide and Dichalcogenides. *Adv. Funct. Mater.* **2013**, *23*, 3952–3970. [CrossRef]
11. Akatsuka, K.; Takanashi, G.; Ebina, Y.; Haga, M.-a.; Sasaki, T. Electronic Band Structure of Exfoliated Titanium- and/or Niobium-Based Oxide Nanosheets Probed by Electrochemical and Photoelectrochemical Measurements. *J. Phys. Chem. C* **2012**, *116*, 12426–12433. [CrossRef]
12. Ida, S.; Ogata, C.; Eguchi, M.; Youngblood, W.J.; Mallouk, T.E.; Matsumoto, Y. Photoluminescence of Perovskite Nanosheets Prepared by Exfoliation of Layered Oxides, $K_2Ln_2Ti_3O_{10}$, $KLnNb_2O_7$, and $RbLnTa_2O_7$ (Ln: Lanthanide Ion). *J. Am. Chem. Soc.* **2008**, *130*, 7052–7059. [CrossRef] [PubMed]
13. Maeda, K.; Eguchi, M.; Oshima, T. Perovskite Oxide Nanosheets with Tunable Band-Edge Potentials and High Photocatalytic Hydrogen-Evolution Activity. *Angew. Chem. Int. Ed.* **2014**, *53*, 13164–13168. [CrossRef] [PubMed]
14. Zhou, Y.; Zhang, Y.; Lin, M.; Long, J.; Zhang, Z.; Lin, H.; Wu, J.C.S.; Wang, X. Monolayered Bi2WO6 nanosheets mimicking heterojunction interface with open surfaces for photocatalysis. *Nat. Commun.* **2015**, *6*, 8340. [CrossRef]
15. Sun, Q.; Jia, X.; Wang, X.; Yu, H.; Yu, J. Facile synthesis of porous Bi_2WO_6 nanosheets with high photocatalytic performance. *Dalton Trans.* **2015**, *44*, 14532–14539. [CrossRef] [PubMed]
16. Tae, E.L.; Lee, K.E.; Jeong, J.S.; Yoon, K.B. Synthesis of Diamond-Shape Titanate Molecular Sheets with Different Sizes and Realization of Quantum Confinement Effect during Dimensionality Reduction from Two to Zero. *J. Am. Chem. Soc.* **2008**, *130*, 6534–6543. [CrossRef]
17. Cao, Y.; Guo, S.; Yu, C.; Zhang, J.; Pan, X.; Li, G. Ionic liquid-assisted one-step preparation of ultrafine amorphous metallic hydroxide nanoparticles for the highly efficient oxygen evolution reaction. *J. Mater. Chem. A* **2020**, *8*, 15767–15773. [CrossRef]
18. Li, W.; Qian, X.; Li, J. Phase transitions in 2D materials. *Nat. Rev. Mater.* **2021**, *6*, 829–846. [CrossRef]
19. Zhang, J.; Xie, Y.; Jiang, Q.; Guo, S.; Huang, J.; Xu, L.; Wang, Y.; Li, G. Facile Synthesis of Cobalt Clusters-CoNx Composites: Synergistic Effect Boosts up Electrochemical Oxygen Reduction. *J. Mater. Chem. A* **2022**, *10*, 16920–16927. [CrossRef]
20. Cao, Y.; Su, Y.; Xu, L.; Yang, X.; Han, Z.; Cao, R.; Li, G. Ionic liquids modified oxygen vacancy-rich amorphous FeNi hydroxide nanoclusters on carbon-based materials as an efficient electrocatalyst for electrochemical water oxidation. *J. Energy Chem.* **2022**, *71*, 167–173. [CrossRef]

21. Ali, S.; Raza, A.; Afzal, A.M.; Iqbal, M.W.; Hussain, M.; Imran, M.; Assiri, M.A. Recent Advances in 2D-MXene Based Nanocomposites for Optoelectronics. *Adv. Mater. Interfaces* **2022**, *9*, 2200556. [CrossRef]
22. Raza, A.; Qumar, U.; Rafi, A.A.; Ikram, M. MXene-based nanocomposites for solar energy harvesting. *Sustain. Mater. Technol.* **2022**, *33*, e00462. [CrossRef]
23. Hassan, J.Z.; Raza, A.; Qumar, U.; Li, G. Recent advances in engineering strategies of Bi-based photocatalysts for environmental remediation. *Sustain. Mater. Technol.* **2022**, *33*, e00478. [CrossRef]
24. Shi, Q.; Raza, A.; Xu, L.; Li, G. Bismuth oxyhalide quantum dots modified titanate-necklaces with exceptional population of oxygen vacancies and photocatalytic activity. *J. Colloid Interface Sci.* **2022**, *625*, 750–760. [CrossRef] [PubMed]
25. Zhong, X.; Liu, Y.; Wang, S.; Zhu, Y.; Hu, B. In-situ growth of COF on BiOBr 2D material with excellent visible-light-responsive activity for U(VI) photocatalytic reduction. *Sep. Purif. Technol.* **2021**, *279*, 119627. [CrossRef]
26. Shi, Q.; Zhang, X.; Liu, X.; Xu, L.; Liu, B.; Zhang, J.; Xu, H.; Han, Z.; Li, G. In-situ exfoliation and assembly of 2D/2D g-C_3N_4/TiO_2(B) hierarchical microflower: Enhanced photo-oxidation of benzyl alcohol under visible light. *Carbon* **2022**, *195*, 401–409. [CrossRef]
27. Ikram, M.; Raza, A.; Imran, M.; Ul-Hamid, A.; Shahbaz, A.; Ali, S. Hydrothermal Synthesis of Silver Decorated Reduced Graphene Oxide (rGO) Nanoflakes with Effective Photocatalytic Activity for Wastewater Treatment. *Nanoscale Res. Lett.* **2020**, *15*, 95. [CrossRef] [PubMed]
28. Ikram, M.; Umar, E.; Raza, A.; Haider, A.; Naz, S.; Ul-Hamid, A.; Haider, J.; Shahzadi, I.; Hassan, J.; Ali, S. Dye degradation performance, bactericidal behavior and molecular docking analysis of Cu-doped TiO_2 nanoparticles. *RSC Adv.* **2020**, *10*, 24215–24233. [CrossRef]
29. Raza, A.; Ikram, M.; Aqeel, M.; Imran, M.; Ul-Hamid, A.; Riaz, K.N.; Ali, S. Enhanced industrial dye degradation using Co doped in chemically exfoliated MoS_2 nanosheets. *Appl. Nanosci.* **2020**, *10*, 1535–1544. [CrossRef]
30. Raza, A.; Rafiq, A.; Qumar, U.; Hassan, J.Z. 2D hybrid photocatalysts for solar energy harvesting. *Sustain. Mater. Technol.* **2022**, *33*, e00469. [CrossRef]
31. Qumar, U.; Hassan, J.Z.; Bhatti, R.A.; Raza, A.; Nazir, G.; Nabgan, W.; Ikram, M. Photocatalysis vs adsorption by metal oxide nanoparticles. *J. Mater. Sci. Technol.* **2022**, *131*, 122–166. [CrossRef]
32. Alarawi, A.; Ramalingam, V.; He, J.-H. Recent advances in emerging single atom confined two-dimensional materials for water splitting applications. *Mater. Today Energy* **2019**, *11*, 1–23. [CrossRef]
33. Faraji, M.; Yousefi, M.; Yousefzadeh, S.; Zirak, M.; Naseri, N.; Jeon, T.H.; Choi, W.; Moshfegh, A.Z. Two-dimensional materials in semiconductor photoelectrocatalytic systems for water splitting. *Energy Environ. Sci.* **2019**, *12*, 59–95. [CrossRef]
34. Wang, G.; Chang, J.; Tang, W.; Xie, W.; Ang, Y.S. 2D materials and heterostructures for photocatalytic water-splitting: A theoretical perspective. *J. Phys. D Appl. Phys.* **2022**, *55*, 293002. [CrossRef]
35. Raza, A.; Hassan, J.Z.; Mahmood, A.; Nabgan, W.; Ikram, M. Recent advances in membrane-enabled water desalination by 2D frameworks: Graphene and beyond. *Desalination* **2022**, *531*, 115684. [CrossRef]
36. Raza, A.; Zhang, X.; Ali, S.; Cao, C.; Rafi, A.A.; Li, G. Photoelectrochemical Energy Conversion over 2D Materials. *Photochem* **2022**, *2*, 272–298. [CrossRef]
37. Raza, A.; Altaf, S.; Ali, S.; Ikram, M.; Li, G. Recent advances in carbonaceous sustainable nanomaterials for wastewater treatments. *Sustain. Mater. Technol.* **2022**, *32*, e00406. [CrossRef]
38. Raza, A.; Ikram, M.; Qumar, U.; Rafiq, A. Hybrid 2D Nanomaterials for Photocatalytic Degradation of Wastewater Pollutants. In *Innovative Nanocomposites for the Remediation and Decontamination of Wastewater*; Kumar, A., Ed.; IGI Global: Hershey, PA, USA, 2022; pp. 101–125.
39. Li, G.; Raza, A.; Ali, S.; Li, Z. MXene-Based Nanocomposite Photocatalysts for Wastewater Treatment. In *Innovative Nanocomposites for the Remediation and Decontamination of Wastewater*; Kumar, A., Ed.; IGI Global: Hershey, PA, USA, 2022; pp. 53–81.
40. Raza, A.; Ikram, M.; Guo, S.; Baiker, A.; Li, G. Green Synthesis of Dimethyl Carbonate from CO_2 and Methanol: New Strategies and Industrial Perspective. *Adv. Sustain. Syst.* **2022**, *6*, 2200087. [CrossRef]
41. Raza, A.; Hassan, J.Z.; Ikram, M.; Naz, S.; Haider, A.; Ul-Hamid, A.; Shahzadi, I.; Haider, J.; Goumri-Said, S.; Kanoun, M.B.; et al. Molecular docking and DFT analyses of magnetic cobalt doped MoS_2 and BN nanocomposites for catalytic and antimicrobial explorations. *Surf. Interfaces* **2021**, *27*, 101571. [CrossRef]
42. Xie, Z.; Peng, Y.-P.; Yu, L.; Xing, C.; Qiu, M.; Hu, J.; Zhang, H. Solar-Inspired Water Purification Based on Emerging 2D Materials: Status and Challenges. *Sol. RRL* **2020**, *4*, 1900400. [CrossRef]
43. Jakhar, M.; Kumar, A.; Ahluwalia, P.K.; Tankeshwar, K.; Pandey, R. Engineering 2D Materials for Photocatalytic Water-Splitting from a Theoretical Perspective. *Materials* **2022**, *15*, 2221. [CrossRef]
44. Zhang, X.; Shi, Q.; Liu, X.; Li, J.; Xu, H.; Ding, H.; Li, G. Facile assembly of InVO4/TiO2 heterojunction for enhanced photo-oxidation of benzyl alcohol. *Nanomaterials* **2022**, *12*, 1544. [CrossRef] [PubMed]
45. Su, Q.; Li, Y.; Hu, R.; Song, F.; Liu, S.; Guo, C.; Zhu, S.; Liu, W.; Pan, J. Heterojunction Photocatalysts Based on 2D Materials: The Role of Configuration. *Adv. Sustain. Syst.* **2020**, *4*, 2000130. [CrossRef]
46. Shi, Q.; Qin, Z.; Sharma, S.; Li, G. Recent progress in heterogeneous catalysis over atomically and structurally precise metal nanoclusters. *Chem. Rec.* **2021**, *21*, 879–892. [CrossRef] [PubMed]

47. Chen, Y.; Li, Y.; Chen, W.; Xu, W.; Han, Z.; Waheed, A.; Ye, Z.; Li, G.; Baiker, A. Continuous Dimethyl Carbonate Synthesis from CO_2 and Methanol over BixCe1-xOδ Monoliths: Effect of Bismuth Doping on Population of Oxygen Vacancies, Activity, and Reaction Pathway. *Nano Res.* **2022**, *15*, 1366–1374. [CrossRef]
48. Yan, D.; Li, Y.; Huo, J.; Chen, R.; Dai, L.; Wang, S. Defect Chemistry of Nonprecious-Metal Electrocatalysts for Oxygen Reactions. *Adv. Mater.* **2017**, *29*, 1606459. [CrossRef]
49. Li, H.; Shang, J.; Ai, Z.; Zhang, L. Efficient Visible Light Nitrogen Fixation with BiOBr Nanosheets of Oxygen Vacancies on the Exposed {001} Facets. *J. Am. Chem. Soc.* **2015**, *137*, 6393–6399. [CrossRef] [PubMed]
50. Zhao, Y.; Chen, G.; Bian, T.; Zhou, C.; Waterhouse, G.I.N.; Wu, L.-Z.; Tung, C.-H.; Smith, L.J.; O'Hare, D.; Zhang, T. Defect-Rich Ultrathin ZnAl-Layered Double Hydroxide Nanosheets for Efficient Photoreduction of CO_2 to CO with Water. *Adv. Mater.* **2015**, *27*, 7824–7831. [CrossRef]
51. Kong, X.; Xu, Y.; Cui, Z.; Li, Z.; Liang, Y.; Gao, Z.; Zhu, S.; Yang, X. Defect enhances photocatalytic activity of ultrathin TiO_2 (B) nanosheets for hydrogen production by plasma engraving method. *Appl. Catal. B Environ.* **2018**, *230*, 11–17. [CrossRef]
52. Liang, L.; Li, X.; Zhang, J.; Ling, P.; Sun, Y.; Wang, C.; Zhang, Q.; Pan, Y.; Xu, Q.; Zhu, J.; et al. Efficient infrared light induced CO_2 reduction with nearly 100% CO selectivity enabled by metallic CoN porous atomic layers. *Nano Energy* **2020**, *69*, 104421. [CrossRef]
53. Lei, F.; Sun, Y.; Liu, K.; Gao, S.; Liang, L.; Pan, B.; Xie, Y. Oxygen Vacancies Confined in Ultrathin Indium Oxide Porous Sheets for Promoted Visible-Light Water Splitting. *J. Am. Chem. Soc.* **2014**, *136*, 6826–6829. [CrossRef] [PubMed]
54. Liu, Y.; Cheng, H.; Lyu, M.; Fan, S.; Liu, Q.; Zhang, W.; Zhi, Y.; Wang, C.; Xiao, C.; Wei, S.; et al. Low Overpotential in Vacancy-Rich Ultrathin CoSe2 Nanosheets for Water Oxidation. *J. Am. Chem. Soc.* **2014**, *136*, 15670–15675. [CrossRef]
55. Pan, L.; Wang, S.; Mi, W.; Song, J.; Zou, J.-J.; Wang, L.; Zhang, X. Undoped ZnO abundant with metal vacancies. *Nano Energy* **2014**, *9*, 71–79. [CrossRef]
56. Wang, S.; Pan, L.; Song, J.-J.; Mi, W.; Zou, J.-J.; Wang, L.; Zhang, X. Titanium-Defected Undoped Anatase TiO_2 with p-Type Conductivity, Room-Temperature Ferromagnetism, and Remarkable Photocatalytic Performance. *J. Am. Chem. Soc.* **2015**, *137*, 2975–2983. [CrossRef] [PubMed]
57. Wang, J.; Jiang, W.; Liu, D.; Wei, Z.; Zhu, Y. Photocatalytic performance enhanced via surface bismuth vacancy of $Bi_6S_2O_{15}$ core/shell nanowires. *Appl. Catal. B Environ.* **2015**, *176–177*, 306–314. [CrossRef]
58. Jiao, X.; Chen, Z.; Li, X.; Sun, Y.; Gao, S.; Yan, W.; Wang, C.; Zhang, Q.; Lin, Y.; Luo, Y.; et al. Defect-Mediated Electron–Hole Separation in One-Unit-Cell $ZnIn_2S_4$ Layers for Boosted Solar-Driven CO_2 Reduction. *J. Am. Chem. Soc.* **2017**, *139*, 7586–7594. [CrossRef]
59. Song, Y.; Wang, H.; Xiong, J.; Guo, B.; Liang, S.; Wu, L. Photocatalytic hydrogen evolution over monolayer $H_{1.07}Ti_{1.73}O_4{\cdot}H_2O$ nanosheets: Roles of metal defects and greatly enhanced performances. *Appl. Catal. B Environ.* **2018**, *221*, 473–481. [CrossRef]
60. Gao, S.; Gu, B.; Jiao, X.; Sun, Y.; Zu, X.; Yang, F.; Zhu, W.; Wang, C.; Feng, Z.; Ye, B.; et al. Highly Efficient and Exceptionally Durable CO_2 Photoreduction to Methanol over Freestanding Defective Single-Unit-Cell Bismuth Vanadate Layers. *J. Am. Chem. Soc.* **2017**, *139*, 3438–3445. [CrossRef]
61. Guan, M.; Xiao, C.; Zhang, J.; Fan, S.; An, R.; Cheng, Q.; Xie, J.; Zhou, M.; Ye, B.; Xie, Y. Vacancy Associates Promoting Solar-Driven Photocatalytic Activity of Ultrathin Bismuth Oxychloride Nanosheets. *J. Am. Chem. Soc.* **2013**, *135*, 10411–10417. [CrossRef]
62. Zhang, G.; Hu, Z.; Sun, M.; Liu, Y.; Liu, L.; Liu, H.; Huang, C.-P.; Qu, J.; Li, J. Formation of Bi_2WO_6 Bipyramids with Vacancy Pairs for Enhanced Solar-Driven Photoactivity. *Adv. Funct. Mater.* **2015**, *25*, 3726–3734. [CrossRef]
63. Di, J.; Zhao, X.; Lian, C.; Ji, M.; Xia, J.; Xiong, J.; Zhou, W.; Cao, X.; She, Y.; Liu, H.; et al. Atomically-thin Bi_2MoO_6 nanosheets with vacancy pairs for improved photocatalytic CO_2 reduction. *Nano Energy* **2019**, *61*, 54–59. [CrossRef]
64. Liu, Y.; Liang, L.; Xiao, C.; Hua, X.; Li, Z.; Pan, B.; Xie, Y. Promoting Photogenerated Holes Utilization in Pore-Rich WO_3 Ultrathin Nanosheets for Efficient Oxygen-Evolving Photoanode. *Adv. Energy Mater.* **2016**, *6*, 1600437. [CrossRef]
65. Di, J.; Chen, C.; Yang, S.-Z.; Ji, M.; Yan, C.; Gu, K.; Xia, J.; Li, H.; Li, S.; Liu, Z. Defect engineering in atomically-thin bismuth oxychloride towards photocatalytic oxygen evolution. *J. Mater. Chem. A* **2017**, *5*, 14144–14151. [CrossRef]
66. Dong, G.; Chen, D.; Luo, J.; Zhu, Y.; Zeng, Y.; Wang, C. Voids padding induced further enhancement in photocatalytic performance of porous graphene-like carbon nitride. *J. Hazard. Mater.* **2017**, *335*, 66–74. [CrossRef]
67. Sun, Y.; Liu, Q.; Gao, S.; Cheng, H.; Lei, F.; Sun, Z.; Jiang, Y.; Su, H.; Wei, S.; Xie, Y. Pits confined in ultrathin cerium(IV) oxide for studying catalytic centers in carbon monoxide oxidation. *Nat. Commun.* **2013**, *4*, 2899. [CrossRef]
68. Jing, Y.; Heine, T. Two-dimensional $Pd_3P_2S_8$ semiconductors as photocatalysts for the solar-driven oxygen evolution reaction: A theoretical investigation. *J. Mater. Chem. A* **2018**, *6*, 23495–23501. [CrossRef]
69. Qiao, M.; Liu, J.; Wang, Y.; Li, Y.; Chen, Z. PdSeO3 Monolayer: Promising Inorganic 2D Photocatalyst for Direct Overall Water Splitting Without Using Sacrificial Reagents and Cocatalysts. *J. Am. Chem. Soc.* **2018**, *140*, 12256–12262. [CrossRef] [PubMed]
70. Lv, X.; Wei, W.; Sun, Q.; Li, F.; Huang, B.; Dai, Y. Two-dimensional germanium monochalcogenides for photocatalytic water splitting with high carrier mobility. *Appl. Catal. B Environ.* **2017**, *217*, 275–284. [CrossRef]
71. Wang, B.; Wang, X.; Yuan, H.; Zhou, T.; Chang, J.; Chen, H. Direct Z-scheme photocatalytic overall water splitting on two dimensional $MoSe_2/SnS_2$ heterojunction. *Int. J. Hydrog. Energy* **2020**, *45*, 2785–2793. [CrossRef]
72. Xu, M.; Yao, S.; Rao, D.; Niu, Y.; Liu, N.; Peng, M.; Zhai, P.; Man, Y.; Zheng, L.; Wang, B.; et al. Insights into Interfacial Synergistic Catalysis over Ni@TiO_{2-x} Catalyst toward Water–Gas Shift Reaction. *J. Am. Chem. Soc.* **2018**, *140*, 11241–11251. [CrossRef] [PubMed]

73. Akimov, A.V.; Jinnouchi, R.; Shirai, S.; Asahi, R.; Prezhdo, O.V. Theoretical Insights into the Impact of Ru Catalyst Anchors on the Efficiency of Photocatalytic CO_2 Reduction on Ta_2O_5. *J. Phys. Chem. B* **2015**, *119*, 7186–7197. [CrossRef]
74. Qin, Y.; Li, H.; Lu, J.; Feng, Y.; Meng, F.; Ma, C.; Yan, Y.; Meng, M. Synergy between van der waals heterojunction and vacancy in $ZnIn_2S_4$/g-C_3N_4 2D/2D photocatalysts for enhanced photocatalytic hydrogen evolution. *Appl. Catal. B Environ.* **2020**, *277*, 119254. [CrossRef]
75. Yang, W.; Zhang, L.; Xie, J.; Zhang, X.; Liu, Q.; Yao, T.; Wei, S.; Zhang, Q.; Xie, Y. Enhanced Photoexcited Carrier Separation in Oxygen-Doped $ZnIn_2S_4$ Nanosheets for Hydrogen Evolution. *Angew. Chem. Int. Ed.* **2016**, *55*, 6716–6720. [CrossRef]
76. Du, C.; Zhang, Q.; Lin, Z.; Yan, B.; Xia, C.; Yang, G. Half-unit-cell $ZnIn_2S_4$ monolayer with sulfur vacancies for photocatalytic hydrogen evolution. *Appl. Catal. B Environ.* **2019**, *248*, 193–201. [CrossRef]
77. Guan, Z.; Xu, Z.; Li, Q.; Wang, P.; Li, G.; Yang, J. AgIn5S8 nanoparticles anchored on 2D layered $ZnIn_2S_4$ to form 0D/2D heterojunction for enhanced visible-light photocatalytic hydrogen evolution. *Appl. Catal. B Environ.* **2018**, *227*, 512–518. [CrossRef]
78. He, Z.; Tang, J.; Shen, J.; Chen, J.; Song, S. Enhancement of photocatalytic reduction of CO_2 to CH_4 over TiO_2 nanosheets by modifying with sulfuric acid. *Appl. Surf. Sci.* **2016**, *364*, 416–427. [CrossRef]
79. Jiang, Z.; Miao, W.; Zhu, X.; Yang, G.; Yuan, Z.; Chen, J.; Ji, X.; Kong, F.; Huang, B. Modifying lewis base on TiO_2 nanosheets for enhancing CO_2 adsorption and the separation of photogenerated charge carriers. *Appl. Catal. B Environ.* **2019**, *256*, 117881. [CrossRef]
80. Liang, L.; Li, X.; Sun, Y.; Tan, Y.; Jiao, X.; Ju, H.; Qi, Z.; Zhu, J.; Xie, Y. Infrared Light-Driven CO_2 Overall Splitting at Room Temperature. *Joule* **2018**, *2*, 1004–1016. [CrossRef]
81. Li, S.; Bai, L.; Ji, N.; Yu, S.; Lin, S.; Tian, N.; Huang, H. Ferroelectric polarization and thin-layered structure synergistically promoting CO_2 photoreduction of Bi_2MoO_6. *J. Mater. Chem. A* **2020**, *8*, 9268–9277. [CrossRef]
82. Li, M.; Cui, Z.; Li, E. Silver-modified MoS_2 nanosheets as a high-efficiency visible-light photocatalyst for water splitting. *Ceram. Int.* **2019**, *45*, 14449–14456. [CrossRef]
83. Li, X.; Sun, Y.; Xu, J.; Shao, Y.; Wu, J.; Xu, X.; Pan, Y.; Ju, H.; Zhu, J.; Xie, Y. Selective visible-light-driven photocatalytic CO_2 reduction to CH_4 mediated by atomically thin $CuIn_5S_8$ layers. *Nat. Energy* **2019**, *4*, 690–699. [CrossRef]
84. Sun, Y.; Sun, Z.; Gao, S.; Cheng, H.; Liu, Q.; Piao, J.; Yao, T.; Wu, C.; Hu, S.; Wei, S.; et al. Fabrication of flexible and freestanding zinc chalcogenide single layers. *Nat. Commun.* **2012**, *3*, 1057. [CrossRef] [PubMed]
85. Sun, Y.; Cheng, H.; Gao, S.; Sun, Z.; Liu, Q.; Liu, Q.; Lei, F.; Yao, T.; He, J.; Wei, S.; et al. Freestanding Tin Disulfide Single-Layers Realizing Efficient Visible-Light Water Splitting. *Angew. Chem. Int. Ed.* **2012**, *51*, 8727–8731. [CrossRef] [PubMed]
86. Su, J.; Li, G.-D.; Li, X.-H.; Chen, J.-S. 2D/2D Heterojunctions for Catalysis. *Adv. Sci.* **2019**, *6*, 1801702. [CrossRef] [PubMed]
87. Di, J.; Yan, C.; Handoko, A.D.; Seh, Z.W.; Li, H.; Liu, Z. Ultrathin two-dimensional materials for photo- and electrocatalytic hydrogen evolution. *Mater. Today* **2018**, *21*, 749–770. [CrossRef]
88. Ganguly, P.; Harb, M.; Cao, Z.; Cavallo, L.; Breen, A.; Dervin, S.; Dionysiou, D.D.; Pillai, S.C. 2D Nanomaterials for Photocatalytic Hydrogen Production. *ACS Energy Lett.* **2019**, *4*, 1687–1709. [CrossRef]
89. Ganguly, P.; Byrne, C.; Breen, A.; Pillai, S.C. Antimicrobial activity of photocatalysts: Fundamentals, mechanisms, kinetics and recent advances. *Appl. Catal. B Environ.* **2018**, *225*, 51–75. [CrossRef]
90. Ida, S.; Ishihara, T. Recent Progress in Two-Dimensional Oxide Photocatalysts for Water Splitting. *J. Phys. Chem. Lett.* **2014**, *5*, 2533–2542. [CrossRef]
91. Parsons, R. The rate of electrolytic hydrogen evolution and the heat of adsorption of hydrogen. *Trans. Faraday Soc.* **1958**, *54*, 1053–1063. [CrossRef]
92. Hinnemann, B.; Moses, P.G.; Bonde, J.; Jørgensen, K.P.; Nielsen, J.H.; Horch, S.; Chorkendorff, I.; Nørskov, J.K. Biomimetic Hydrogen Evolution: MoS_2 Nanoparticles as Catalyst for Hydrogen Evolution. *J. Am. Chem. Soc.* **2005**, *127*, 5308–5309. [CrossRef]
93. Zhang, Y.-H.; Li, Y.-L.; Jiu, B.-B.; Gong, F.-L.; Chen, J.-L.; Fang, S.-M.; Zhang, H.-L. Highly enhanced photocatalytic H_2 evolution of Cu_2O microcube by coupling with TiO_2 nanoparticles. *Nanotechnology* **2019**, *30*, 145401. [CrossRef] [PubMed]
94. Bi, W.; Ye, C.; Xiao, C.; Tong, W.; Zhang, X.; Shao, W.; Xie, Y. Spatial Location Engineering of Oxygen Vacancies for Optimized Photocatalytic H_2 Evolution Activity. *Small* **2014**, *10*, 2820–2825. [CrossRef] [PubMed]
95. Li, J.; Zhan, G.; Yu, Y.; Zhang, L. Superior visible light hydrogen evolution of Janus bilayer junctions via atomic-level charge flow steering. *Nat. Commun.* **2016**, *7*, 11480. [CrossRef] [PubMed]
96. Xu, Q.; Zhu, B.; Jiang, C.; Cheng, B.; Yu, J. Constructing 2D/2D Fe_2O_3/g-C_3N_4 Direct Z-Scheme Photocatalysts with Enhanced H_2 Generation Performance. *Sol. RRL* **2018**, *2*, 1800006. [CrossRef]
97. Ran, J.; Jaroniec, M.; Qiao, S.-Z. Cocatalysts in Semiconductor-based Photocatalytic CO_2 Reduction: Achievements, Challenges, and Opportunities. *Adv. Mater.* **2018**, *30*, 1704649. [CrossRef]
98. Sun, Z.; Wang, H.; Wu, Z.; Wang, L. g-C_3N_4 based composite photocatalysts for photocatalytic CO_2 reduction. *Catal. Today* **2018**, *300*, 160–172. [CrossRef]
99. Chang, X.; Wang, T.; Gong, J. CO_2 photo-reduction: Insights into CO_2 activation and reaction on surfaces of photocatalysts. *Energy Environ. Sci.* **2016**, *9*, 2177–2196. [CrossRef]
100. Marszewski, M.; Cao, S.; Yu, J.; Jaroniec, M. Semiconductor-based photocatalytic CO_2 conversion. *Mater. Horiz.* **2015**, *2*, 261–278. [CrossRef]
101. Surdhar, P.S.; Mezyk, S.P.; Armstrong, D.A. Reduction potential of the carboxyl radical anion in aqueous solutions. *J. Phys. Chem.* **1989**, *93*, 3360–3363. [CrossRef]

102. Inoue, T.; Fujishima, A.; Konishi, S.; Honda, K. Photoelectrocatalytic reduction of carbon dioxide in aqueous suspensions of semiconductor powders. *Nature* **1979**, *277*, 637–638. [CrossRef]
103. Lin, S.-C.; Chang, C.-C.; Chiu, S.-Y.; Pai, H.-T.; Liao, T.-Y.; Hsu, C.-S.; Chiang, W.-H.; Tsai, M.-K.; Chen, H.M. Operando time-resolved X-ray absorption spectroscopy reveals the chemical nature enabling highly selective CO_2 reduction. *Nat. Commun.* **2020**, *11*, 3525. [CrossRef] [PubMed]
104. Jiang, M.-P.; Huang, K.-K.; Liu, J.-H.; Wang, D.; Wang, Y.; Wang, X.; Li, Z.-D.; Wang, X.-Y.; Geng, Z.-B.; Hou, X.-Y.; et al. Magnetic-Field-Regulated TiO_2 {100} Facets: A Strategy for C-C Coupling in CO_2 Photocatalytic Conversion. *Chem* **2020**, *6*, 2335–2346. [CrossRef]
105. Maeda, K. Metal-Complex/Semiconductor Hybrid Photocatalysts and Photoelectrodes for CO_2 Reduction Driven by Visible Light. *Adv. Mater.* **2019**, *31*, 1808205. [CrossRef] [PubMed]
106. Xiong, J.; Song, P.; Di, J.; Li, H. Ultrathin structured photocatalysts: A versatile platform for CO_2 reduction. *Appl. Catal. B Environ.* **2019**, *256*, 117788. [CrossRef]
107. Xu, S.; Carter, E.A. Theoretical Insights into Heterogeneous (Photo)electrochemical CO_2 Reduction. *Chem. Rev.* **2019**, *119*, 6631–6669. [CrossRef] [PubMed]
108. Qin, D.; Zhou, Y.; Wang, W.; Zhang, C.; Zeng, G.; Huang, D.; Wang, L.; Wang, H.; Yang, Y.; Lei, L.; et al. Recent advances in two-dimensional nanomaterials for photocatalytic reduction of CO_2: Insights into performance, theories and perspective. *J. Mater. Chem. A* **2020**, *8*, 19156–19195. [CrossRef]
109. Kattel, S.; Liu, P.; Chen, J.G. Tuning Selectivity of CO_2 Hydrogenation Reactions at the Metal/Oxide Interface. *J. Am. Chem. Soc.* **2017**, *139*, 9739–9754. [CrossRef]
110. Ginés, M.J.L.; Marchi, A.J.; Apesteguía, C.R. Kinetic study of the reverse water-gas shift reaction over $CuO/ZnO/Al_2O_3$ catalysts. *Appl. Catal. A Gen.* **1997**, *154*, 155–171. [CrossRef]
111. Rihko-Struckmann, L.K.; Peschel, A.; Hanke-Rauschenbach, R.; Sundmacher, K. Assessment of Methanol Synthesis Utilizing Exhaust CO_2 for Chemical Storage of Electrical Energy. *Ind. Eng. Chem. Res.* **2010**, *49*, 11073–11078. [CrossRef]
112. Wang, F.; Wei, M.; Evans, D.G.; Duan, X. CeO_2-based heterogeneous catalysts toward catalytic conversion of CO_2. *J. Mater. Chem. A* **2016**, *4*, 5773–5783. [CrossRef]
113. Khalil, M.; Gunlazuardi, J.; Ivandini, T.A.; Umar, A. Photocatalytic conversion of CO_2 using earth-abundant catalysts: A review on mechanism and catalytic performance. *Renew. Sustain. Energy Rev.* **2019**, *113*, 109246. [CrossRef]
114. Wang, Y.; He, D.; Chen, H.; Wang, D. Catalysts in electro-, photo- and photoelectrocatalytic CO_2 reduction reactions. *J. Photochem. Photobiol. C Photochem. Rev.* **2019**, *40*, 117–149. [CrossRef]
115. Fu, Z.; Yang, Q.; Liu, Z.; Chen, F.; Yao, F.; Xie, T.; Zhong, Y.; Wang, D.; Li, J.; Li, X.; et al. Photocatalytic conversion of carbon dioxide: From products to design the catalysts. *J. CO_2 Util.* **2019**, *34*, 63–73. [CrossRef]
116. Sun, Z.; Talreja, N.; Tao, H.; Texter, J.; Muhler, M.; Strunk, J.; Chen, J. Catalysis of Carbon Dioxide Photoreduction on Nanosheets: Fundamentals and Challenges. *Angew. Chem. Int. Ed.* **2018**, *57*, 7610–7627. [CrossRef]
117. White, J.L.; Baruch, M.F.; Pander, J.E.; Hu, Y.; Fortmeyer, I.C.; Park, J.E.; Zhang, T.; Liao, K.; Gu, J.; Yan, Y.; et al. Light-Driven Heterogeneous Reduction of Carbon Dioxide: Photocatalysts and Photoelectrodes. *Chem. Rev.* **2015**, *115*, 12888–12935. [CrossRef]
118. Liang, L.; Lei, F.; Gao, S.; Sun, Y.; Jiao, X.; Wu, J.; Qamar, S.; Xie, Y. Single Unit Cell Bismuth Tungstate Layers Realizing Robust Solar CO_2 Reduction to Methanol. *Angew. Chem. Int. Ed.* **2015**, *54*, 13971–13974. [CrossRef]
119. Tonda, S.; Kumar, S.; Bhardwaj, M.; Yadav, P.; Ogale, S. g-C_3N_4/NiAl-LDH 2D/2D Hybrid Heterojunction for High-Performance Photocatalytic Reduction of CO_2 into Renewable Fuels. *ACS Appl. Mater. Interfaces* **2018**, *10*, 2667–2678. [CrossRef]
120. Jo, W.-K.; Kumar, S.; Eslava, S.; Tonda, S. Construction of Bi_2WO_6/RGO/g-C_3N_4 2D/2D/2D hybrid Z-scheme heterojunctions with large interfacial contact area for efficient charge separation and high-performance photoreduction of CO_2 and H_2O into solar fuels. *Appl. Catal. B Environ.* **2018**, *239*, 586–598. [CrossRef]
121. Cao, S.; Shen, B.; Tong, T.; Fu, J.; Yu, J. 2D/2D Heterojunction of Ultrathin MXene/Bi2WO6 Nanosheets for Improved Photocatalytic CO_2 Reduction. *Adv. Funct. Mater.* **2018**, *28*, 1800136. [CrossRef]
122. Ye, M.; Wang, X.; Liu, E.; Ye, J.; Wang, D. Cover Feature: Boosting the Photocatalytic Activity of P25 for Carbon Dioxide Reduction by using a Surface-Alkalinized Titanium Carbide MXene as Cocatalyst (ChemSusChem 10/2018). *ChemSusChem* **2018**, *11*, 1577. [CrossRef]
123. Li, N.; Chen, X.; Ong, W.-J.; MacFarlane, D.R.; Zhao, X.; Cheetham, A.K.; Sun, C. Understanding of Electrochemical Mechanisms for CO_2 Capture and Conversion into Hydrocarbon Fuels in Transition-Metal Carbides (MXenes). *ACS Nano* **2017**, *11*, 10825–10833. [CrossRef] [PubMed]
124. Bai, Y.; Ye, L.; Chen, T.; Wang, L.; Shi, X.; Zhang, X.; Chen, D. Facet-Dependent Photocatalytic N_2 Fixation of Bismuth-Rich Bi_5O_7I Nanosheets. *ACS Appl. Mater. Interfaces* **2016**, *8*, 27661–27668. [CrossRef] [PubMed]
125. Liu, C.; Xu, Q.; Zhang, Q.; Zhu, Y.; Ji, M.; Tong, Z.; Hou, W.; Zhang, Y.; Xu, J. Layered BiOBr/Ti_3C_2 MXene composite with improved visible-light photocatalytic activity. *J. Mater. Sci.* **2019**, *54*, 2458–2471. [CrossRef]